THE PHYSICS OF ORIGAMI

A Dissertation
Presented to
The Academic Faculty

By

James McInerney

In Partial Fulfillment
of the Requirements for the Degree
Doctor of Philosophy in the
School of Physics

Georgia Institute of Technology

August 2021

THE PHYSICS OF ORIGAMI

Thesis committee:

Dr. D. Zeb Rocklin
School of Physics
Georgia Institute of Technology

Dr. Alberto Fernandez-Nieves
School of Physics
Georgia Institute of Technology

Dr. Elisabetta Matsumoto
School of Physics
Georgia Institute of Technology

Dr. Daniel I. Goldman
School of Physics
Georgia Institute of Technology

Dr. Glaucio H. Paulino
Department of Civil Engineering
Georgia Institute of Technology

Dr. Predrag Cvitanovic
School of Physics
Georgia Institute of Technology

Date approved: August 2021

Because no battle is ever won he said. They are not even fought. The field only reveals to man his own folly and despair, and victory is an illusion of philosophers and fools.

William Faulkner

In memory of James Tilley

ACKNOWLEDGMENTS

I must express my most sincere appreciation to Zeb Rocklin who was able to combat my stubborness so that I could become a better version of myself and who patiently pushed me to get there.

I have assembled my committee with those whom I most wish to emulate as a physicist and for that I am indebted to all the inspiration they have given me: to Glaucio Paulino with his devotion to excellence in every practice; to Sabetta Matusmoto with her ability to convey the transcendental; to Alberto Fernandez-Nieves with his infectious energy and passion for science; to Dan Goldman with his unfathomable level of productivity; and to Predrag Cvitanovic with his all-inclusive and everlasting quest for learning.

There are countless others that have influenced my life over the past half decade, including my friends and family who have been forced to accept my extended absence and annual reappearances. I wish to thank explicitly the people whom I believe have had a direct impact on this thesis: to Brian Kennedy and Roman Grigoriev from whom I learned the "theoretical" part of my career as a physicist is more important than the subfield; to Michael Dimitriev who first directed me towards soft condensed matter; to Perry Ellis who taught me to take responsibility for my own work; to Michael Czjakowski whose consistent insight has improved the quality of my research; to Alasdair Gent whose ears I regularly commandeered to express to new ideas; and to Chris Crowley for innumerable philosphical musings from which I better understand where my niche fits in the broad scope of science.

Lastly, I would like to acknowledge my own shortcomings, particularly an excess of arrogance and a lack of humility, and hope this thesis serves as my penance since the graduate experience was most humbling.

SUMMARY

The physics of origami concerns the relationship between the introduction of creases to a thin sheet and their influence on the mechanical response of the sheet. In many cases, the kinematics are well-approximated by treating the origami sheet as completely rigid and imposing geometric compatibility conditions, similar to Lagrange multipliers, that permit folding of the sheet provided the faces are not deformed. In the linear regime, these rigid modes are governed by a compatibility matrix, similar to a quantum Hamiltonian, whose symmetry properties govern the existence and features of the modes. Most of the existing literature has focused on particular examples of crease patterns and there is a lack of general statements on the relationship between crease geometry and mechanical response.

In this thesis, I explore two broad classes of periodic origami sheet: those whose unit cells are composed of all (any number) triangular faces and those whose unit cells are composed of four parallelogram faces. For the triangulations I show that a hidden symmetry guarantees the existence of a two-dimensional space of degenerate ground states, through which the sheet can rigidly fold, and enforces a realness condition on the compatibility matrix so that periodically triangulated origami belongs to a special topological class of materials. For the parallelograms I show that a discrete symmetry divides the compatibility matrix into symmetric and antisymmetric sectors of modes and moreover, that these mode symmetries lead to distinct mechanical responses: the symmetric mode generates exclusively in-plane strains while the antisymmetric mode generates exclusively out-of-plane curvatures. These efforts form a basis for the classification of periodic origami by the symmetries of their compatibility matrices that may be extended to other systems such as spin magnets and mechanical metamaterials.

TABLE OF CONTENTS

LIST OF FIGURES

CHAPTER 1
INTRODUCTION

The term "origami" is typically associated with the art of folding paper into static configurations by the careful process of folding creases. Recently, this art has become a science dedicated to understanding how a crease pattern can be designed to control the properties of a sheet [1], including exotic mechanical response [2, 3, 4, 5, 6, 7, 8, 9, 10, 11]. While the rich behavior of the underlying material influences such properties, the behavior of many origami-inspired structures is well-approximated by geometric compatibility constraints [12, 3, 13]. Nonetheless, determining whether a particular three-dimensional shape can be rigidly folded from a particular crease pattern is NP-hard [14] due to long-range coupling and combinatoric ordering. Still, linear deformations of origami sheets are well-characterized by the null space of its linear compatibility matrix in the same way quantum wavefunctions are characterized by eigenstates of their Hamiltonian. Thus, I study the physics of origami by considering classes of crease patterns distinguished by the symmetry properties of their linear compatibility matrices, similar to the ten-fold classification of topological insulators and superconductors [15, 16, 17, 18, 19].

Origami is the special case of thin sheets where deformations are localized to predefined creases. Generically, thin sheets are geometrically constrained by the equations of Gauss and Codazzi that couple in-plane strains with out-of-plane curvatures [20], two deformations that typically are governed by distinct elastic moduli so that this feature can be manipulated to generate a variety of morphological structures by stretching or compressing local regions of the sheet [21]. The one-dimensional creases and zero-dimensional vertices of origami naturally arise via stress localization in thin sheets under strong external fields [22] giving rise to the formation of periodic patterns such as the zig-zag instability resulting from biaxial compression [23, 24, 25, 26, 27, 28, 29]. Remarkably, when this pattern of

creases is folded onto an origami sheet, the mechanical response of the sheet is dominated by the dilation that generates the instability [30, 31].

Indeed, this process of encoding form [32] and function via crease geometry is viable in macroscopic shape-memory alloys [33, 34, 35, 36], microscopic polymer sheets [37, 38, 39, 40, 41, 42, 43, 44, 45, 46], and atomically thin graphene [47, 48] and plasmene [49] so that under mild external fields these materials self-fold into the programmed shape despite the distinct material properties and length scales. The scale-free and material independent behavior arises because stretching deformations have an elastic modulus that scales linearly with the thickness and are hence suppressed relative to bending deformations which have an elastic modulus that scales as the thickness cubed [50]. Thus, for sufficiently thin origami sheets, the modes of deformation are dominated by the isometries (deformations that preserve length) and the complex elasticity of the sheets [51, 52, 53] can be ignored.

Such origami sheets are referred to as *rigid origami* and are governed by geometric compatibility conditions [54, 55, 13] that are more tractable than continuum models for analytical and numerical [56] computations. These models have been primarily explored on a case-by-case basis by picking crease geometries with symmetry properties that simplify analysis [57] and it is not clear how their properties change when these symmetries are broken [58, 59]. While this approach has been able to identify crease patterns with degenerate ground states (rigidly foldable configurations) [60], negative Poisson ratios [2, 61, 5, 6], and high stiffness-to-weight ratios [8, 7], the symmetries responsible for these properties have not been formalized in the manner done within other areas of physics. Consequently, the current literature is unable to provide intuitive reasoning for the relationship between a crease pattern and the resulting mechanical response so that new crease patterns must be designed via creative ingenuity or brute-force computational algorithms [32].

In this thesis, I address this gap by exploring two broad classes of periodic origami via symmetry arguments. First, I consider triangulations whose isometries approximate the low-energy response of non-triangulated crease patterns [3, 13]. I show that these triangula-

tions exhibit a hidden symmetry which couples the left and right null spaces of the compatibility matrix, thereby leading to a two-dimensional space of degenerate ground states and unique topological properties. Second, I consider crease patterns whose unit cells are composed of four parallelogram faces which generalizes several well-known crease patterns [2, 61, 5, 6]. I show that this family of crease patterns exhibits a discrete symmetry that decomposes the compatibility matrix into symmetric and antisymmetric sectors, thereby constraining the linear response so that there always exists a single negative Poisson ratio mode. These efforts are not meant to be all inclusive but instead to provide a formalism that can be applied to classify crease patterns by the properties of their compatibility matrix and hence, develop intuition for their mechanical response.

The contents of this thesis are as follows. In chapter 2, I review the theory of rigidity in the context of frames to provide simple examples of the tools that I apply for the study of origami. In chapter 3, I introduce the geometric compatibility conditions for rigid origami and explore the implications of the hidden symmetry for periodic triangulations. In chapter 4, I introduce compatibility constraints on the linear isometries of parallelogram origami and explore the implications of the discrete symmetry for the particular case with four faces. In chapter 5, I review the progress made on triangulations and parallelograms and discuss the extension to future work.

CHAPTER 2
A REVIEW ON THE RIGIDITY OF FRAMES

The theory of rigidity concerns the ability of mechanical structures to support external loads or be deformed. While seemingly elementary, the general practices of this field apply to a vast number of systems and provide insight to many physical phenomenon including jamming [62, 63] and rigidity percolation [64, 65, 66]. My treatment of origami as *rigid* origami is one particular example. Here, I review the rigidity of frames composed of masses connected by harmonic springs to develop intuition for the analysis of origami. I focus on the aspects which directly parallel to the forthcoming analysis and omit many of the generalizing features.

2.1 The rigidity of free frames

Frames are consider *free* if they have open boundaries such as the classical example of a truss. Despite these open boundaries, such free frames can be rigid due to constraints on their edges. Here, I discuss the existence of such modes at first (subsection 2.1.1) and second (subsection 2.1.2) order in the vertex displacements as well as the implications of force-bearing modes (subsection 2.1.3) and symmetries (subsection 2.1.4).

2.1.1 Linear zero modes

A frame is first-order rigid if there are no infinitesimal displacements of the vertices which preserve the edge lengths to first order. Indexing each vertex by the lowercase Latin letters, i, and each edge as the pair of vertices which it connects, (i, j), the edge vector is

$$\mathbf{r}_{(i,j)} = \mathbf{r}_j - \mathbf{r}_i. \tag{2.1}$$

For an infinitesimal displacement of the vertices, $\mathbf{r}_i \to \mathbf{r}_i + \epsilon \mathbf{u}_i$, where $\epsilon \ll 1$, this vector is generically extended or compressed by the amount

$$e_{(i,j)} = \hat{r}_{(i,j)} \cdot (\mathbf{u}_j - \mathbf{u}_i) + O(\epsilon^2). \tag{2.2}$$

For a frame with V vertices and E edges in d-dimensions, the array of all edge extensions, $\mathbf{e} = \begin{pmatrix} \dots e_{(i,j)} \dots \end{pmatrix}$, is given by a linear map from the array of all vertex displacements, $\mathbf{U} = \begin{pmatrix} \dots \mathbf{u}_i \dots \end{pmatrix}$, call the rigidity matrix

$$\mathbf{e} = \mathbf{R}\mathbf{U}. \tag{2.3}$$

Note, the array of vertex displacements contains d components for each vertex. This rigidity matrix has dV rows and E columns so that it generically has a $dV - E$-dimensional null space spanned by the *linear zero modes*: vertex displacements that do not stretch any bonds. However, this null space includes the $d(d+1)/2$ global symmetries of the embedding space. This counting argument dates back to Maxwell [67], though requires modification when the rigidity matrix is not full rank as I discuss in subsection 2.1.3.

For example, consider the triangular and quadrilateral frames embedded in the two-dimensional Euclidean plane Figure 2.1(a) and (c). The triangle consists of three sites and three bonds yielding a total of six degrees of freedom and three constraints. These three remaining degrees of freedom correspond to the two rigid translations and one rigid rotation of the Euclidean plane so that the triangle is rigid, also called *isostatic*. In contrast, the quadrilateral frame consists of four sites and four bonds yielding a total of eight degrees of freedom and four constraints. Of these remaining four degrees of freedom, there is one non-trivial linear zero mode that corresponds to shearing the quadrilateral frame an infinitesimal amount. I discuss in section 2.2 the extension to periodic frames that is more relevant to the study of periodic origami.

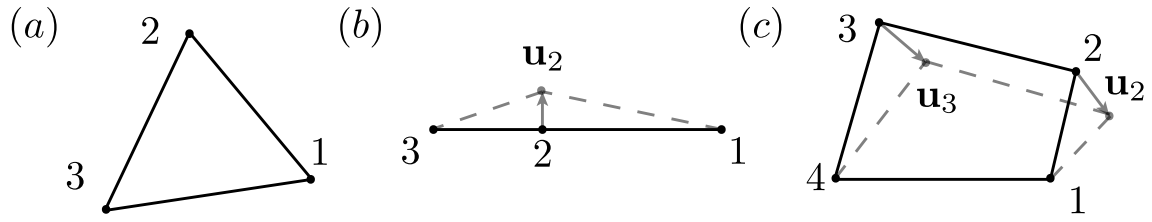

Figure 2.1: Examples of free frames. (a) A triangle in the Euclidean plane has three vertices, each with two degrees of freedom, and three edges for a total of $6 - 3 = 3$ degrees of freedom. These remaining 3 degrees of freedom are the two Euclidean translations and one Euclidean rotation so that the triangle has no linear zero modes. (b) A triangle in the Euclidean plane with all of its edges parallel has degenerate to first order so that it exhibits a linear zero mode but always extends the edges to second order so that it is second-order rigid. (c) A quadrilateral in the Euclidean plane has four vertices, each with two degrees of freedom, and four edges for a total of $8 - 4 = 4$ degrees of freedom. These remaining 4 degrees of freedom correspond to the three Euclidean symmetries mentioned in (a) along with one linear zero mode that corresponds to shearing the quadrilateral.

2.1.2 Second-order rigidity

The existence of linear zero modes implies a frame is not first-order rigid however, it does not imply the frame is not rigid. This is because there may be a degeneracy in the first-order constraints so that they are trivially satisfied while higher-order constraints rigidify the frame [68]. Expanding the edge lengths to second-order in the vertex displacements and denoting the second-order contribution to these displacements as $\dot{\mathbf{u}}$ yields

$$e_{(i,j)} = \hat{r}_{(i,j)} \cdot (\dot{\mathbf{u}}_j - \dot{\mathbf{u}}_i) + (\mathbf{u}_j - \mathbf{u}_i) \cdot (\mathbf{u}_j - \mathbf{u}_i) + O(\epsilon^3), \tag{2.4}$$

where it is assumed the $\mathbf{u}_i$ are linear zero modes so that the first-order extensions vanish. This can be interpreted as a constraint on the linear combinations of linear zero modes, $\mathbf{U} = \sum_\mu \lambda_\mu \mathbf{U}_\mu$, to ensure the existence of quadratic zero modes.

For example, consider the triangular frame in the flattened state as well as the quadrilateral frame embedded in the two-dimensional Euclidean plane as shown in Figure 2.1(b) and (c). The bonds of the triangular frame are aligned so that any vertex displacement orthogonal to this line is a linear zero mode. However, this always yields an extension at

second-order so that this particular configuration of the triangular frame is second-order rigid. In contrast, the one linear zero mode of the quadrilateral frame generically exhibits a second-order correction so that it is not second-order rigid. In fact, quadrilateral frames generically exhibit *finite mechanisms* which transform them nonlinearly throughout the embedding space [69, 70], a feature similar to four-coordinated origami vertices that is exploited in chapter 4. For less simplified systems where there exist multiple linear zero modes, these second-order constraints can lead to bifurcations in the configuration space as shown in section 3.3 for periodically triangulated origami.

2.1.3 States of self stress

The counting of linear zero modes by Maxwell assumes that the rigidity matrix is full rank. However, this is not always the case. Importantly, the left null space of the rigidity matrix is physically meaningful as it is spanned by the *states of self stress*: assignments of tension that maintain equilibrium in the frame [71]. Assuming the edges function as harmonic springs, such tensions, $t_{(i,j)}$, sum to yield the force on a vertex

$$\mathbf{f}_i = \sum_{j'} t_{(i,j')} \hat{r}_{(i,j')}, \tag{2.5}$$

where the sum is taken over all vertices j' connected to vertex i. Similarly to the construction of the rigidity matrix, the array of net forces on each vertex $\mathbf{F} = \begin{pmatrix} \dots \mathbf{f}_i \dots \end{pmatrix}$ is given by a linear map on the array of edge tensions $\mathbf{t} = \begin{pmatrix} \dots t_{(i,j)} \dots \end{pmatrix}$ called the *equilibrium matrix*

$$\mathbf{F} = \mathbf{Q}\mathbf{t}, \tag{2.6}$$

whose null space is spanned by the states of self stress. Note, similar to the array of vertex displacements, the array of net forces contains d elements for force. By inspection, this equilibrium matrix is exactly the transpose of the rigidity matrix, $\mathbf{Q} = \mathbf{R}^T$, (a feature

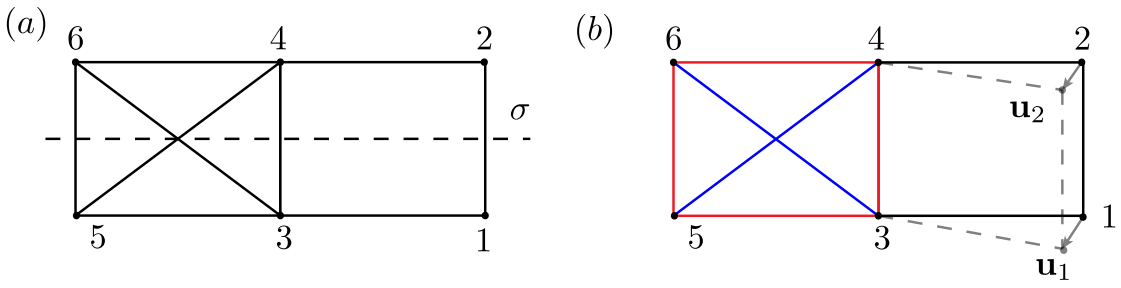

Figure 2.2: Example of a symmetric frame. (a) Two quadrilateral frames where one has additional cross beams. This frame has a reflection symmetry indicated by σ so its linear zero modes and states of self stress must be symmetric or antisymmetric under this symmetry. (b) This frame exhibits a state of self stress where edges in the left quadrilateral have tension assignments (indicated by red) with the opposite sign of those assigned to the cross beams (indicated by blue) which is symmetric under the reflection σ. This frame also exhibits a linear zero mode where the right quadrilateral shears which is antisymmetric under the reflection σ. The existence of these force-bearing and zero modes follows from the static-kinematic duality that yields the Maxwell-Calladine index theorem.

referred to as the static-kinematic duality [72, 73]) so that the existence of states of self stress increases the number of linear zero modes as exhibited by the Maxwell-Calladine index theorem

$$N_{ZM} - N_{SS} = dV - E, \tag{2.7}$$

where N_{ZM} and N_{SS} respectively refer to the number of zero modes and number of states of self stress [71].

For example, consider the connected quadrilateral frames shown in Figure 2.2(a) where one has two cross beams. This frame has six vertices and nine edges so that there are only three remaining degrees of freedom which correspond to the three continuous symmetries of the Euclidean plane. However, the existence of the cross beams allows the left quadrilateral to support external loads, thereby generating a state of self stress where the cross beams and the edges in the left quadrilateral have tension assignments of opposite sign. Hence, there exists a single linear zero mode that corresponds to the shearing of the quadrilateral on the right. The existence of such states of self stress takes a more significant role for

periodic frames in section 2.2 where they explain the ability of frames with equal numbers of constraints and degrees of freedom to deform by changing their periodicity. Moreover, the equilibrium condition on these states of self stress is, in fact, identical to the linear constraint on triangulated origami as shown in chapter 3 and gives rise to a connection between the rigidy body modes of origami to its linear isometries.

2.1.4 Discrete symmetries

Discrete symmetries provide an alternative, and more informative, analysis of the frame in Figure 2.2(a) than that in subsection 2.1.3. Clearly, this frame has a reflection symmetry, as indicated by σ, that can be used to block-diagonalize the rigidity and equilibrium matrices [74, 75]. Each block then exhibits its own counting argument where the zero modes and states of self stress of a particular block are equisymmetric to the constraints and degrees of freedom of that block [76, 77]. I demonstrate this with a lack of rigour simply to emphasize the role of discrete symmetries on the linear response of mechanical systems.

For example, this frame is invariant under the group composed of the identity element, E, and the reflection element, σ, so that the counting should be performed in the irreducible representations $A = (E, \sigma)$ and $A' = (E, -\sigma)$. For the degrees of freedom, there are 12 total, none of which are invariant under the reflection while there are 3 continuous symmetries, one of which is invariant under the reflection so that there are $5A + 4A'$ remaining degrees of freedom. For the constraints, there are 9 total, 3 of which are invariant under the reflection for a total of $6A + 3A'$ constraints. Thus, the difference between the number of linear zero modes and states of self stress is $-A + A'$, indicating there is one symmetric state of self stress and one antisymmetric linear zero mode. Moreover, these symmetries can also be used to guarantee the modes extend beyond first order [78]. This ability to decompose linear operators into blocks corresponding to particular symmetries is vital to the analysis of the four-parallelogram origami in chapter 4.

2.2 The rigidity of periodic frames

Often, it is convenient to consider the bulk response of a material by imposing periodic boundary conditions. There has recently been extensive interest in the study of such periodic frames due to a generalization of Bloch-waves that leads to a correspondence between analysis of the bulk and boundary modes [79, 73, 72]. Here, I discuss uniform and nonuniform modes in periodic frames along with the conditions for topologically protected modes.

2.2.1 Uniform modes in periodic frames

A frame embedded in Euclidean space extends to a periodic frame by making an association between opposite sides e.g. edges emanating from the right of the frame are associated with those entering the left of the frame. Such a frame can be described by the *unit cell* of minimal vertices and edges that are repeated along with the *lattice vectors*, $\boldsymbol{\ell}_\mu$, that translate one cell to its neighbor as shown in Figure 2.3(a). This association means periodic frames in the Euclidean plane are topologically equivalent a torus hence, their number of vertices, edges, and faces are related by the Euler characteristic

$$\chi = V - E + F, \tag{2.8}$$

which vanishes, $\chi = 0$, for tori. The primary interest here is in frames that are the periodic equivalent of isostatic (called *Maxwell*) where, in two dimensions, $E = 2V$ so that there are equal numbers of constraints and degrees of freedom and, by Euler's formula in Equation 2.8, there are $F = V$ faces.

Regardless of whether a periodic frame is Maxwell, the uniform linear zero modes lie in the null space of the quotiented rigidity matrix that maps the displacement of vertices in the unit cell to the extensions of edges in the unit cell. Importantly, the lattice vectors indicate continuous translational symmetries that correspond to linear zero modes in periodic frames. However, the number of such lattice vectors is less than the number of possible

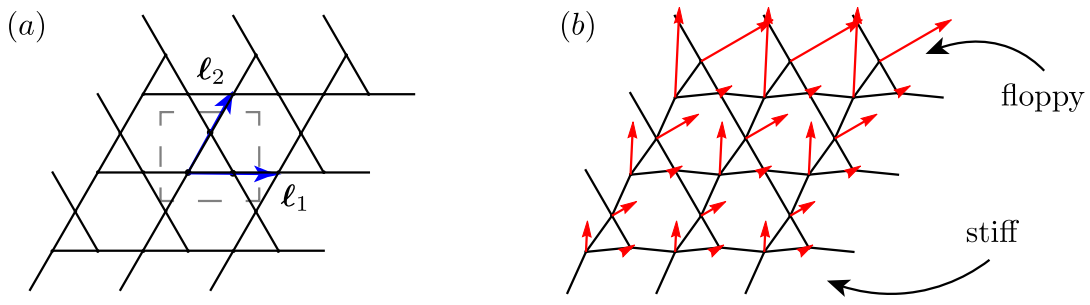

Figure 2.3: The kagome lattice as an example of a periodic frame. (a) The untwisted kagome lattice is composed of triangles and hence, can support external stresses so that despite being critically coordinated it exhibits deformations that correspond to changes in its periodicity. (b) The kagome lattice can be topologically polarized so that one side has exponentially localized floppy modes while the other is stiff.

loads the frame could resolve; for example, in the Euclidean plane there are the two uniaxial stresses in addition to shear stress. Thus, Maxwell frames that can support external loads exhibit more states of self stress and hence, by the Maxwell-Calladine index theorem, must possess an additional linear zero mode [80]. Such linear zero modes correspond to changes in the periodicity [81] and are often referred to as the Guest-Hutchinson modes. This relationship is crucial to the investigation of Maxwell origami in chapter 3 with the distinction the left null space of the compatibility matrix is instead spanned by the rigid body modes.

2.2.2 Nonuniform modes in periodic frames

More generally, the linear zero modes and states of self stress in periodic frames are nonuniform. However, the periodicity implies that they must be described by generalized Bloch factors

$$\mathbf{U}(\mathbf{n}) = \mathbf{U}(0,0) z_1^{n^1} z_2^{n^2}, \tag{2.9}$$

$$\mathbf{t}(\mathbf{n}) = \mathbf{t}(0,0) z_1^{n^1} z_2^{n^2}, \tag{2.10}$$

where $\mathbf{n} = (n^1, n^2)$ specifies the cell of the frame and $z_\mu = \exp^{iq_\mu}$ are the Bloch factors [82] with generically complex wavenumbers q_μ. Similar to the study of electromagnetic waves, the real part of this wavenumber corresponds to sinusoidally varying deformations while the complex part corresponds to evanescent waves that are exponentially localized.

In this case, the formula for edge extensions (vertex forces) include a factor of z_μ for every vertex (edge) that belongs to a cell in the n^μ direction. Thus, the rigidity and equilibrium matrices are wavenumber dependent (a feature that arises by taking the Fourier transform of the matrix defined over the entire frame and noting that the modes belong to orthogonal sectors). However, by inspection these wavenumber dependencies are opposite and the Maxwell-Calladine index theorem becomes [73, 72]

$$N_{ZM}(\mathbf{q}) - N_{SS}(-\mathbf{q}) = dV - E. \tag{2.11}$$

Importantly, this means linear zero modes exponentially localied to one edge are paired with states of self stress exponentially localized to the opposite edge; an intuitive feature that means when one side of the frame is floppy, the other side is generically stiff as shown in Figure 2.3(b).

The existence of a linear zero mode or a state of self stress at a particular wave number means that the determinant of the, respectively, rigidity or equilibrium matrix must vanish at this wavenumber. This determinant is generically a complex number and hence, it can be described by an amplitude and a phase. By the Cauchy residue theorem, the integral of this phase over Bloch factors of unit magnitude counts the difference in the number of zeroes with Bloch factors that have less than and greater than unit magnitude. The corresponding wavenumbers respectively have positive and negative imaginary components, $k = \mathrm{Im}q$, indicating that they are exponentially localized on opposite sides. This yields the topological index, called the *winding number*, that determines e.g. the difference in the

number of modes on the left and right boundaries of the frame [79]

$$\nu = \frac{1}{2i\pi} \oint dq \frac{d}{dq} \mathrm{Im} \ln \det \mathbf{R}(q), \tag{2.12}$$

where the wavenumber in the transverse direction is held fixed and the integral is taken over a closed loop in the Brillouin zone: the 2π periodic space of real-valued wavenumbers which is isomorphic to a torus. Such topological invariants have been used to predict *topological polarization* in a number of mechanical systems at the Maxwell point [79, 70, 83, 84, 85] however, in a numerical study the winding number was found to always vanish for periodically triangulated origami [86]. I show in section 3.2 that this is due to a hidden symmetry in origami that pairs exponentially localized modes on opposites sides of the sheet so that Maxwell origami belongs to a different topological class than Maxwell frames [88] which also includes spin magnets [89]. More generically, the winding number is the first homotopy group of rigidity matrix where the nth homotopy group of a map computes the number of times the n-sphere covers the map. This same homotopy theory can be used to quantify the existence of topological defects in superfluid and nematic phases by defining maps over the real space representation of the system [87], as opposed to the reciprocal space for the present case given by the Brillouin zone, where for a d-dimensional medium, a m-dimensional defect is classified by the $d - m - 1$ homotopy group.

2.3 Discussion

I have presented several aspects regarding the rigidity of frames as simpler examples of tools that I later apply to rigid origami. In particular, I discussed the existence of linear zero modes in frames as a consequence of excess degrees of freedom as well as a consequence of the pairing with states of self stress. Next, I presented second-order conditions that constrain these linear zero modes and permit a frame to be second-order rigid. Following, I showed how discrete symmetries can constrain the properties of linear zero modes and

states of self stress. Lastly, I reviewed recent work on topologically protected states.

CHAPTER 3

TRIANGULATIONS AND ORIGAMI'S HIDDEN SYMMETRY

The onset of mechanical criticality, where the number of constraints in a system equals the number of degrees of freedom, is associated with the jamming transition [63]. For polyhedra, this corresponds to a triangulation of the surface, which is known to be generically rigid [90]. Here, I use a hidden symmetry connecting two different descriptions of linear zero modes to show periodically triangulated origami, called *Maxwell origami*, has a two-dimensional space of rigidly-foldable, screw-periodic configurations and belongs to a distinct topological class that requires edge modes to arise in pairs on opposite sides of the sheet.

Triangulated origami is most conveniently parameterized by specifying the angles between crease-sharing faces, called *fold angles* (which are the complements of the dihedral angles), constrained by compatibility conditions that ensure closed paths on the surface do not rotate elements of the origami sheet relative to themselves [54, 55]. For periodic origami, such compatibility conditions impose constraints on the periodicity, whose vertices are not generically spatially periodic but instead *screw-periodic* so that the orientation of edges and faces are rotated between cells, and the origami sheet approximates a cylindrical surface [91]. Infinitesimal changes to these fold angles are identical to the equilibrium condition for assignments of tensions to a frame composed of the same edges [90, 92] so that, in addition to the mechanical criticality of Maxwell origami, there is a self-duality.

Here, I investigate the properties of this combined criticality and duality as done in my PNAS [93]. I modify the Maxwell-Calladine index theorem to pair zero modes described by changes in the vertex position with those described by changes in the fold angles, thereby revealing the existence of a uniform, linear folding zero mode for every rigid body mode and the fact that exponentially localized edge modes arise in pairs localized to opposite

sides of the sheet. These two features explain the two-dimensional space of rigidly foldable cylindrical configurations predicted by Tachi [91] along with the lack of topological polarization observed in a numerical study Chen et al [86]. Furthermore, I show that similar to developable vertices [94], spatially periodic origami sheets branch between upwards and downwards folded configuration spaces.

The content of this chapter, which is based on my publication [93], is organized as follows. In section 3.1, I introduce the vertex compatibility condition and discuss the consequent screw periodicity of origami. In section 3.2, I examine constraints on the infinitesimal changes to the fold angles and discuss the existence of such folding motions that are compatible with the crease pattern along with their implications, including the topological properties of Maxwell origami. In section 3.3, I derive constraints on the first-order folding motions that determine when they extend to second order and hence, can branch the configuration space. In section 3.4, I numerically confirm the analysis of the previous sections by constructing a two-dimensional space of rigidly foldable cylindrical configurations that branches from the spatially-periodic configuration. In section 3.5, I summarize the results of this section and discuss avenues for further work.

3.1 Compatibility and screw-periodic vertices

Similar to the way that the fixed edge lengths determine the admissible vertex positions in a rigid frame, the fixed interior angles, called *sector angles*, determine the admissible fold angles in a rigid origami sheet. Arbitrary paths in the sheet are composed of rotations across faces and about edges so that the orthonormal frame of an observer is transformed as they move along the sheet. However, these rotations must vanish over any closed path so that no element of the sheet is rotated relative to itself. This yields the rigid origami compatibility condition first introduced by belcastro and Hull [55] that extends to intercellular compatibility conditions restricting periodic assignments of sector and fold angles to yield cylindrical sections as first shown by Tachi [91]. Here, I review these arguments in

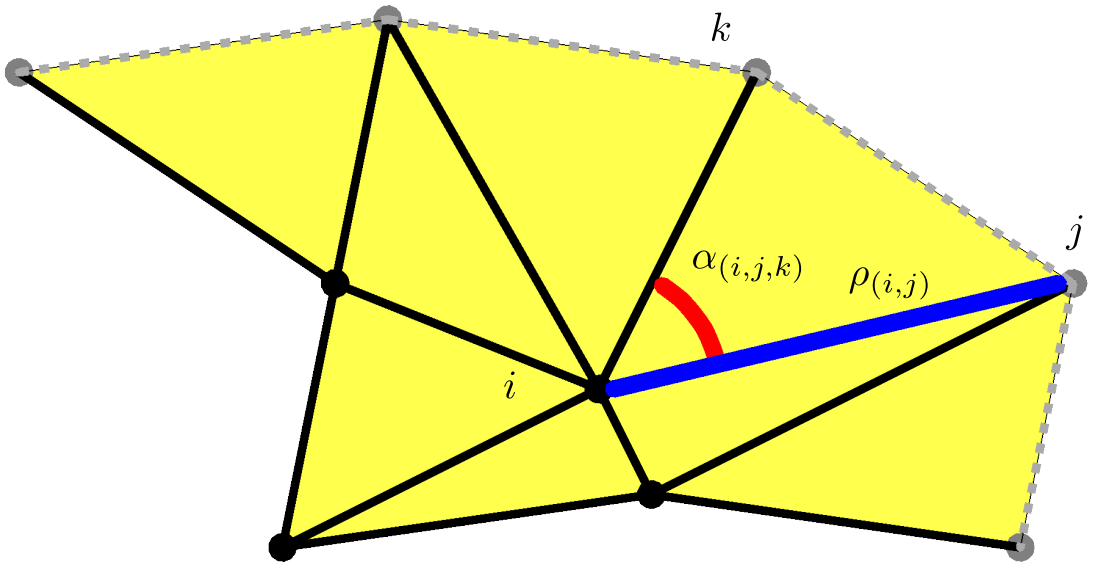

Figure 3.1: Vertices are denoted via their lowercase Latin index, edges are denoted by the pairs of vertices they adjoin, and faces are denoted by the triplet of vertices they bound. The angle between edges (i, j) and (i, k), called the sector angle, is denoted $\alpha_{(i,j,k)}$ and the fold angle between faces (i, j, l) and (i, j, k) is denoted $\rho_{(i,j)}$.

subsection 3.1.1 and subsection 3.1.2 respectively.

First, let me introduce the notation shown in Figure 3.1. I denote individual vertices via their lowercase Latin index, edges by the pairs of vertices they adjoin, and faces by the triplet of vertices they bound. The angle between edges (i, j) and (i, k), called the *sector angle*, is denoted $\alpha_{(i,j,k)}$ and the fold angle between faces (i, j, l) and (i, j, k) is denoted $\rho_{(i,j)}$.

3.1.1 Vertex compatibility

Consider the closed path around a particular vertex and the resulting transformations on the direction of edge (i, j_1) and face normal (i, j_1, j_2). The edges are successively rotated about the normal vector of each face while the face normals are successively rotated about each edge. Since the faces are not necessarily co-planar, the corresponding rotation axes

have a complicated, implicit dependence on the sector angles and fold angles. Still, each of these rotations can be written in the initial frame by using an appropriate similarity transformation, thereby yielding a closed-form constraint on the admissible fold angles.

This similarity transformation is obtained via the rotation between adjacent frames. Without loss of generality, consider the transformation from the frame at edge (i, j_1) and face (i, j_1, j_2) to that at edge (i, j_2) and face (i, j_2, j_3)

$$\mathbf{P}_{(i,j_1,j_2)} \equiv \mathbf{R}_{\hat{n}_{(i,j_1,j_2)}}(\alpha_{(i,j_1,j_2)})\mathbf{R}_{\hat{r}_{(i,j_1)}}(\rho_{(i,j_2)}), \tag{3.1}$$

$$\hat{r}_{(i,j_2)} = \mathbf{P}_{(i,j_1,j_2)}\hat{r}_{(i,j_1)}, \tag{3.2}$$

$$\hat{n}_{(i,j_2,j_3)} = \mathbf{P}_{(i,j_1,j_2)}\hat{n}_{(i,j_1,j_2)}. \tag{3.3}$$

This similarity transformation functions by folding the crease of the new frame in the basis of the previous frame before rotating the crease to its target location. Importantly, this feature can be used to write rotations in the second frame as similarity transformations of those in the first

$$\mathbf{R}_{\hat{r}_{(i,j_2)}}(\rho_{(i,j_2)}) = \mathbf{P}_{(i,j_1,j_2)}\mathbf{R}_{\hat{r}_{(i,j_1)}}(\rho_{(i,j_2)})\mathbf{P}^{-1}_{(i,j_1,j_2)}, \tag{3.4}$$

$$\mathbf{R}_{\hat{n}(i,j_2,j_3)}(\alpha_{(i,j_2,j_3)}) = \mathbf{P}_{(i,j_1,j_2)}\mathbf{R}_{\hat{n}_{(i,j_1,j_2)}}(\alpha_{(i,j_2,j_3)})\mathbf{P}^{-1}_{(i,j_1,j_2)}. \tag{3.5}$$

Thus, because the starting point (i, j_1) was arbitrary, such similarity transformations exist for every component of the closed loop.

Consequently, the vertex compatibility condition can be written as the product of rotations computed within a single frame. In particular, take the frame where edge (i, j_1) is

aligned with the x-axis and face normal (i, j_1, j_2) is aligned with the z-axis to yield

$$\prod_{j',k'} \mathbf{R}_{\hat{z}}(\alpha_{(i,j',k')})\mathbf{R}_{\hat{x}}(\rho_{(i,k')}) = \mathbf{1}, \tag{3.6}$$

where the product is taken in counterclockwise order over every vertex j' connected to vertex i with k' immediately following j'. The fold angles that satisfy this condition at every vertex in an origami sheet specify the rigidly foldable configurations which correspond to a surface of degenerate ground states. However, such solutions are difficult to determine; instead I show in section 3.2 that a hidden symmetry guarantees the existence of linear modes for Maxwell origami and use second-order conditions in section 3.3 along with numerics in section 3.4 to show this surface is two-dimensional.

3.1.2 Periodic angles and screw-periodicity

The vertex compatibility condition in Equation 3.6 ensures that elements of the origami sheet do not rotate relative to theirselves on a closed path around a particular vertex. Since this must hold at every vertex in the origami sheet, the same must be true for arbitrary loops composed of several vertices. This yields compatibility conditions on the generators of the periodic sheet which, in contrast to the spatially-periodic frames, consist of *lattice rotations* in addition to lattice vectors.

Consider an origami sheet satisfying the vertex compatibility condition everywhere. The position of a vertex is translated by the lattice vectors defined as the sum of the edges along any path connecting the vertices

$$\boldsymbol{\ell}_\mu \equiv \mathbf{r}_i(n^\mu = 1) - \mathbf{r}(n^\mu = 0) = \sum_{(i',j')} \mathbf{r}_{(i',j')}. \tag{3.7}$$

However, edges and faces are generically rotated relative to one another by the lattice rota-

tions

$$\begin{aligned} \mathbf{S}_\mu &\equiv \prod_{(i',j')} \mathbf{R}_{(i',j')}(\rho_{(i',j')}), \\ \hat{r}_{(i,j)}(n^\mu = 1) &= \mathbf{S}_\mu \mathbf{r}_{(i,j)}(n^\mu = 0), \\ \hat{n}_{(i,j,k)}(n^\mu = 1) &= \mathbf{S}_\mu \mathbf{r}_{(i,j,k)}(n^\mu = 0). \end{aligned} \tag{3.8}$$

The periodicity of the sector and fold angles imposes constraints on the these lattice vectors and lattice rotations ensuring positions and orientations are path independent.

First, note that the periodicity ensures that the lattice rotations are identical in every cell and that the lattice vectors can only change by a lattice rotation. Thus, two paths connecting cell $\mathbf{n} = (0, 0)$ to cell $\mathbf{n} = (1, 1)$ – traveling first through $\mathbf{n} = (1, 0)$ versus $\mathbf{n} = (0, 1)$ – yield the position and orientation compatibility conditions

$$\boldsymbol{\ell}_1 + \mathbf{S}_1 \boldsymbol{\ell}_2 = \boldsymbol{\ell}_2 + \mathbf{S}_2 \boldsymbol{\ell}_1, \tag{3.9}$$

$$\mathbf{S}_1 \mathbf{S}_2 = \mathbf{S}_2 \mathbf{S}_1. \tag{3.10}$$

The orientation compatibility condition in Equation 3.10 is generically satisfied when the two lattice rotations are about a common axis, here denoted $\hat{s}$, so that position compatibility reduces to a two-dimensional constraint on the components of the lattice vectors transverse to the lattice rotation axis.

This position compatibility condition ensures that transverse components of the lattice vectors, when treated as geometric chords, define a unique radius of curvature. Since the lattice vectors are rotated by an angle θ_μ between cells, the lattice vectors in adjacent cells subtend an angle θ_μ when projected into the plane with normal vector $\hat{s}$. This means that

they are the geometric chords of a circle with radius

$$\kappa_\mu^{-1} = \frac{|\boldsymbol{\ell}_\mu^\perp|}{2\sin\frac{\theta_\mu}{2}}, \tag{3.11}$$

where the superscript $\perp$ denotes the transverse component. The transverse components of Equation 3.9 are invertible, thereby defining the transverse components of one lattice vector in terms of those of the other

$$\boldsymbol{\ell}_2^\perp = \left(\mathbf{1} - \mathbf{S}_1^\perp\right)^{-1}\left(\mathbf{1} - \mathbf{S}_2^\perp\right)\boldsymbol{\ell}_1^\perp, \tag{3.12}$$

which ensures Equation 3.11 is independent of the choice of lattice direction, $\kappa_1 = \kappa_2$.

Thus, the compatibility conditions ensure origami sheets with periodic angle assignments have a unique rotation axis and a unique radius of curvature. Such a sheet approximates a section of a cylinder (and for a tessellation, one that intersects itself an infinite number of times) such as that shown in Figure 3.2, though it does not necessarily yield a closed cylinder such as the origami bellows [95, 96]. The two resulting cylindrical symmetries are crucial to the analytical arguments in section 3.2 and section 3.3 for the existence of first-order and second-order folding motions respectively. Lastly, while the lattice rotations are independent of how the unit cell is defined, the lattice vectors are generically different when defined from a different vertex due to the effective thickness of the corrugated origami sheet; a feature that is used in chapter 4.

3.2 Linear modes and the hidden symmetry

The compatibility condition in Equation 3.6 is difficult to make any analytical statements about. Similar to the rigidity of frames, it is easier to consider whether there exist any infinitesimal perturbations to the fold angles that satisfy vertex compatibility to first order. Such first-order folding motions map to non-uniform vertex displacements and, due to a self-duality unique for triangulations, are isomorphic to states of self stress which are

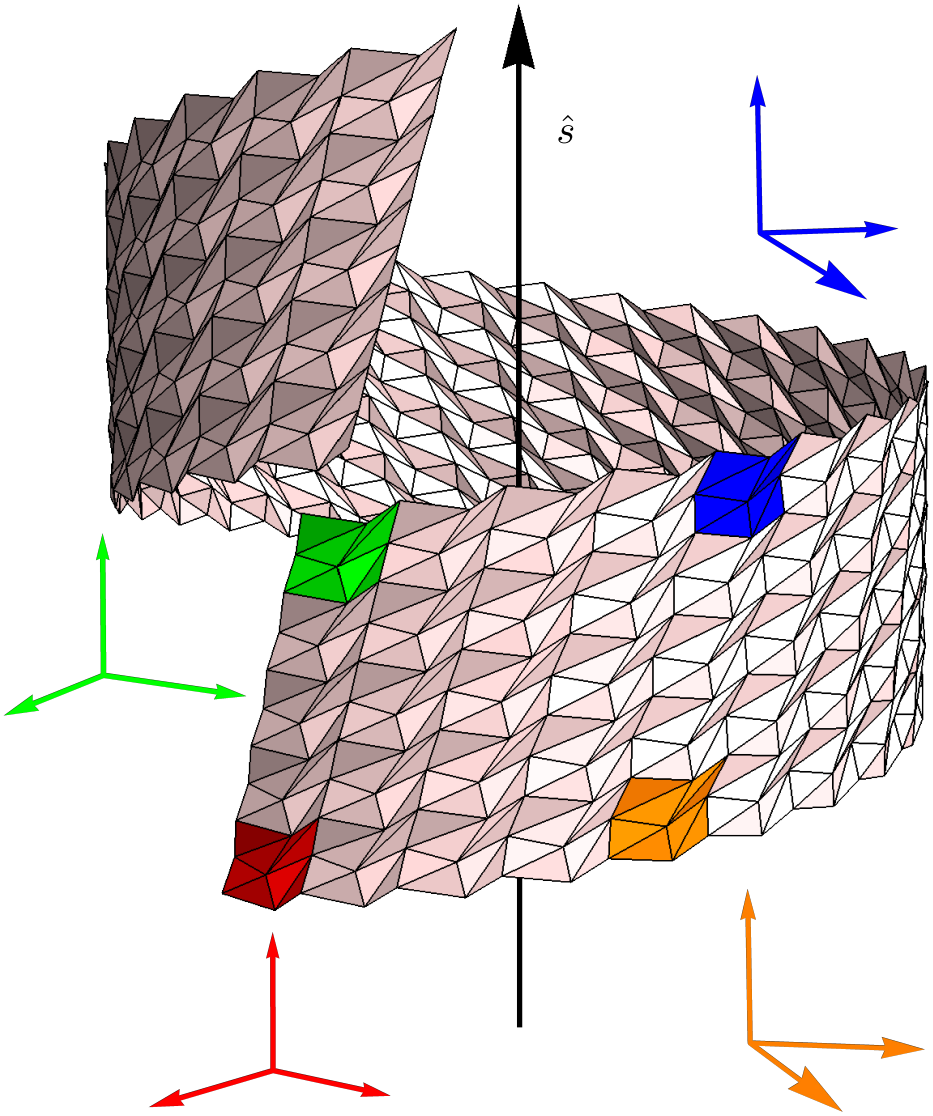

Figure 3.2: Periodic angle assignments generically lead to screw-periodic vertex positions that are characterized by a unique rotation axis and a unique radius of curvature. The consequence is that vectors on the sheet rotate between cells as indicated by the four frames.

paired with vertex zero modes via the Maxwell-Calladine index theorem. This leads to the hidden symmetry of Maxwell origami that pairs uniform first-order folding motions with rigid body modes and also pairs nonuniform modes which are exponentially localized on opposite edges. Here, I expand the vertex compatibility condition to first order in changes to the fold angles as done by Tachi [97], yielding the intuitive, linear constraint equivalent to the equilibrium condition on frames, as explored separately by Gluck [90] and Crapo and Whiteley [92]. I then map between zero modes described by changes in the fold angles to zero modes described by changes in the vertex positions, thereby revealing the hidden symmetry introduced in my PNAS [93] and explaining the lack of topological polarization in Maxwell origami observed numerically by Chen et al [86].

3.2.1 First-order folding motions

Consider an infinitesimal change to the fold angles denoted by $\rho_{(i,j)} \to \rho_{(i,j)} + \epsilon\phi_{(i,j)}$ for $\epsilon \ll 1$. These first-order folding motions cannot rotate elements of the rigid origami sheet relative themselves without deforming the panels, thereby constraining the allowed folding motions. Naturally, such a constraint may be immediately written as the requirement that the sum of the induced generators of rotation vanish on closed paths. For completeness, I show that this result is indeed obtained by expansion of the vertex compatibility condition Equation 3.6.

The expansion of the vertex compatibility condition to first-order in ϵ is

$$\sum_{j''} \phi_{(i,j'')} \prod_{j'=j''} \Big(\mathbf{R}_{\hat{z}}(\alpha_{(i,j',k')})\mathbf{R}_{\hat{x}}(\rho_{(i,j')})\Big)\boldsymbol{\sigma}_{\hat{x}}^{(1)} \prod^{j'=j''-1} \Big(\mathbf{R}_{\hat{z}}(\alpha_{(i,j',k')})\mathbf{R}_{\hat{x}}(\rho_{(i,j')})\Big) = \mathbf{0}, \tag{3.13}$$

where $\boldsymbol{\sigma}_{\hat{x}}^{(1)}$ is the generator of rotations about the x-axis, the outer sum is taken over all edges emanating from vertex i, and the first (second) product is taken from (up to) edge (i, j''). Recall that these products are exactly the similarity transformations that map a

frame at edge (i, j_1) to one at (i, j'') and moreover, by the vertex compatibility condition they must be the inverse of one another. Hence, this condition is equivalent to the sum of the generators of rotation about each edge emanating from vertex i. Thus, because the generators of rotation are skew-symmetric, this is equivalent to the vector condition

$$\sum_{j'} \phi_{(i,j')} \hat{r}_{(i,j')} = \mathbf{0}, \tag{3.14}$$

as expected.

These linear vertex compatibility conditions can be concatenated to compose the linear compatibility matrix, $\mathbf{C}$, whose null space is spanned by the first-order folding motions concatenated as $\boldsymbol{\phi}$. Similar to the nonuniform modes of periodic frames in subsection 2.2.2, the first-order folding motions are z-periodic due to a generalization of Bloch waves [82] where changes in the fold angles on creases that connect two cells carry factors of $z_\mu = \exp^{iq_\mu}$ for wavenumber q_μ so that the compatibility matrix is wavenumber-dependent, $\mathbf{C}(\mathbf{q})$, and its determinant vanishes at wavenumbers for which zero modes exist. First-order folding motions for which $\mathbf{q} = (0, 0)$ are called uniform while those for which $\mathbf{q} \neq (0, 0)$ are called nonuniform.

The first-order folding motions induce changes to the periodicity of the origami sheet. In particular, starting from a spatially periodic sheet, the first-order intercellular compatibility conditions are

$$\boldsymbol{\Omega}_1 \times \boldsymbol{\ell}_2 = \boldsymbol{\Omega}_2 \times \boldsymbol{\ell}_1, \tag{3.15}$$

$$\boldsymbol{\Omega}_1 \times \boldsymbol{\Omega}_2 = \boldsymbol{\Omega}_2 \times \boldsymbol{\Omega}_1, \tag{3.16}$$

where $\boldsymbol{\Omega}_\mu$ is the lattice angular velocity that determines the amount the first-order folding motion rotates adjacent cells relative to one another. Importantly, the expansion of the position compatibility condition constraints the lattice angular velocities to lie in the plane of

the sheet spanned by the two lattice vectors. This indicates the expansion of the orientation compatibility condition is effectively one dimensional. The fact that this condition is trivially satisfied to first order is indicative of the branching discussed in section 3.3.

In contrast, this condition is non-degenerate for screw-periodic sheets. Rather than expand the position and orientation compatibility conditions from a generic configuration, it is more instructive to consider the effect of a linear mode on the rotation axis. The new rotation axis must satisfy

$$\mathbf{S}'_\mu \hat{s}'_\mu = (\mathbf{1} + \mathbf{\Omega}^\times_\mu)\mathbf{S}_\mu(\hat{s} + \delta\hat{s}_\mu) = \hat{s}'_\mu, \tag{3.17}$$

where $\mathbf{\Omega}^\times_\mu$ is the skew-symmetric generator of rotations corresponds to the lattice angular velocity. Since $\hat{s}$ is a unit vector, any changes must be rotations of the vector allowing us to consider only the transverse components. In this case, we find at first order

$$(\mathbf{1} - \mathbf{S}^\perp_\mu)\delta\hat{s}^\perp_\mu = (\mathbf{\Omega}^\times_\mu \hat{s})^\perp, \tag{3.18}$$

and, notably, the transverse components of the lattice angular velocity satisfies an identical relation to the transverse components of the lattice vectors due to the path independence of Equation 3.24

$$\delta\hat{s}^\perp_{1,2} = (\mathbf{1} - \mathbf{S}^\perp_{1,2})^{-1}(\mathbf{\Omega}_{1,2} \times \hat{s})^\perp, \tag{3.19}$$

is identical in both lattice directions. Thus, screw-periodic sheets stay screw-periodic; a feature that guarantees first-order folding motions extend to second order as discussed in **??**.

3.2.2 Isomorphism and self-duality

The linear vertex compatibility condition in Equation 3.14 is identical to that for states of self stress in a frame with the same edges. Importantly, this frame is indistinguishable

from the origami because the triangular faces are isostatic so that there is an isomorphism between the first-order folding motions of the origami and the states of self stress of the frame

$$\phi_{(i,j)} \leftrightarrow t_{(i,j)}. \tag{3.20}$$

This self-duality is nontrivial: for non-triangular faces, such as quadrilaterals, the first-order folding motions are instead isomorphic to states of self stress in a different system, namely one that swaps every block with a hole [98].

Thus, the Maxwell-Calladine index theorem that relates the number of zero modes to the number of states of self stress in a frame can be replaced with an index theorem that relates the number of zero modes described by vertex displacements (VZM) to the number of those described by folding motions (FZM). Moreover, since triangulated origami is at the Maxwell point it has equal numbers of constraints and degrees of freedom so that this is an exact equality

$$N_{VZM}(\mathbf{q}) = N_{FZM}(-\mathbf{q}). \tag{3.21}$$

This relationship has two distinct cases: the first for uniform modes when $\mathbf{q} = \mathbf{0}$ and the vertex zero modes cannot be mapped to folding zero modes and the second for nonuniform modes when $\mathbf{q} \neq \mathbf{0}$ and the vertex zero modes can be mapped to folding zero modes. The immediate consequence of the former is that there is a uniform, first-order folding motion for every rigid body mode of the system which is 2 in generic, screw-periodic configurations and 3 in non-generic, spatially-periodic configurations

$$\text{screw-periodic:} \quad N_{FZM} = 2, \tag{3.22}$$

$$\text{spatially-periodic:} \quad N_{FZM} = 3. \tag{3.23}$$

The discrepancy between the number of first-order folding motions arises due to symmetry breaking from the spatially-periodic configuration and is resolved in section 3.3 via quadratic compatibility constraints. The consequence of Equation 3.21 for nonuniform modes is explored in subsection 3.2.4 after explicitly mapping between vertex and folding zero modes in subsection 3.2.3.

3.2.3 Mapping between vertex and folding zero modes

Changes in the fold angles generate rotations of the origami faces, thereby displacing vertices as shown in Figure 3.3. Importantly, the linear compatibility condition Equation 3.14 ensures that these rotations and displacements are well-defined. Moreover, these nonuniform displacements can be inverted, up to global translations and rotations, to determine changes in the fold angles so that the pairing of nonuniform vertex zero modes and nonuniform folding zero modes in Equation 3.21 in fact pairs zero modes (of either type) at opposite wavenumbers. Thus, screw-periodic sheets stay screw-periodic; a feature that guarantees first-order folding motions extend to second order as discussed in **??**.

The rotations generated by a first-order folding motion are described by an angular velocity field defined on the faces whose gradients are localized to creases

$$\boldsymbol{\omega}_{(i,j,k)} - \boldsymbol{\omega}_{(i_0,j_0,k_0)} = \sum_{(i',j')} \phi_{(i',j')} \hat{r}_{(i',j')}, \tag{3.24}$$

where the sum is taken over any path from face (i_0, j_0, k_0) to face (i, j, k), and these faces may generically be in distinct cells. These angular velocity gradients correspond to rotations of faces about shared creases, thereby displacing vertices

$$\mathbf{u}_i - \mathbf{u}_{i_0} = \sum_{(i',j')} \left(\boldsymbol{\omega}_{(i',j',k')} - \boldsymbol{\omega}_{(i_0,j_0,k_0)}\right) \times \mathbf{r}_{(i',j')}, \tag{3.25}$$

where the sum is again taken over any path connecting the two vertices i and i_0, which similarly may be in distinct cells. This formula for the vertex displacement implicitly

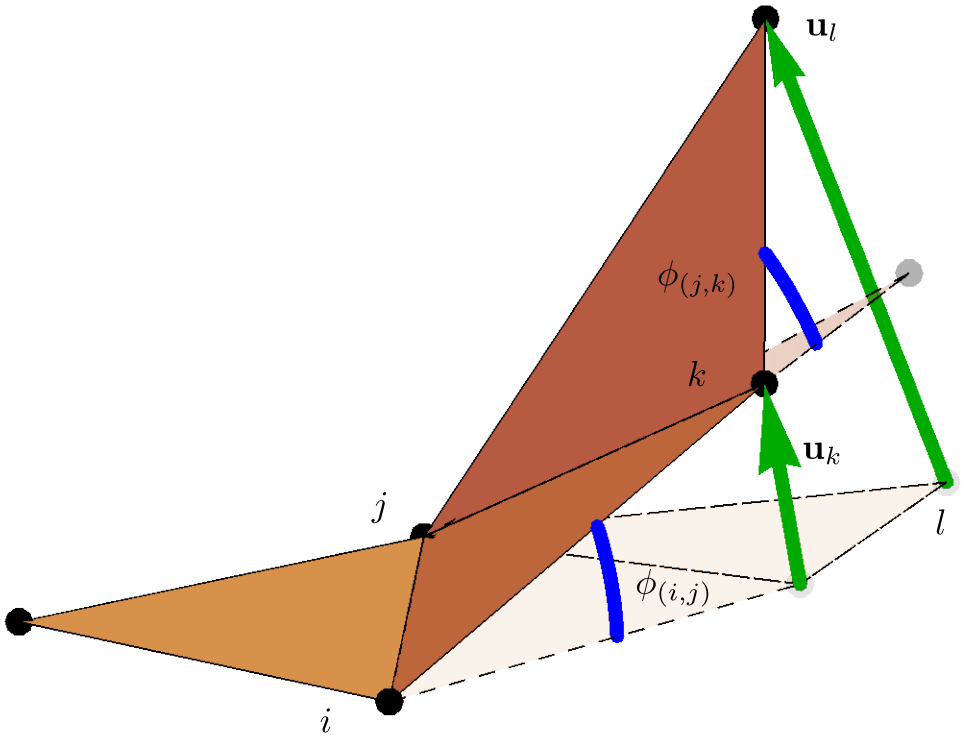

Figure 3.3: First-order folding motions, $\phi_{(i,j)}$, generate rotations characterized by the angular velocity field, $\boldsymbol{\omega}_{(i,j,k)}$, defined in Equation 3.24, thereby displacing vertices by $\mathbf{u}_i$ according to Equation 3.25.

contains a double sum which means that vertex displacements accumulate nonlinearly (in the cell index) across the sheet as shown in Figure 3.3; a hallmark of two-dimensional origami curving in three-dimensional space.

Similarly, vertex displacements that do not stretch any edges can be inverted to determine changes in the fold angles. This is because two face-sharing edges, $\mathbf{r}_{(i,j)}, \mathbf{r}_{(i,k)}$, and their cross product, $\mathbf{n}_{(i,j,k)}$, (the normal vector of the face) are rotated by the same angular velocity

$$\boldsymbol{\omega}^{\times}_{(i,j,k)} \begin{pmatrix} \mathbf{r}_{(i,j)} & \mathbf{r}_{(i,k)} & \mathbf{n}_{(i,j,k)} \end{pmatrix} = \begin{pmatrix} \delta\mathbf{r}_{(i,j)} & \delta\mathbf{r}_{(i,k)} & \delta\mathbf{n}_{(i,j,k)} \end{pmatrix}, \tag{3.26}$$

where δ denotes the infinitesimal change as computed by the vertex displacements in Equation 3.25 and $\boldsymbol{\omega}^{\times}_{(i,j,k)}$ is the skew-symmetric matrix representing the angular velocity. The matrix of the initial edge vectors and the normal vector is generically invertible to yield the angular velocity. Hence, this process can be repeatedly applied to determine changes in the fold angles that correspond to a set of nonuniform vertex displacements.

The connection between zero modes described by changes in the fold angles and changes in the vertex positions described by Equation 3.25 and Equation 3.26 indicate first-order folding motions are paired with vertex zero modes. Moreover, these connections arise at the same wavenumber so that Equation 3.21 becomes

$$N_{VZM}(\mathbf{q}) = N_{VZM}(-\mathbf{q}), \tag{3.27}$$

which is the *hidden symmetry* of Maxwell origami: independent of any spatial symmetries, zero modes appear in pairs at opposite wavenumber. This hidden symmetry has consequences for the topological classification of the compatibility matrix for Maxwell origami which I discuss in subsection 3.2.4.

3.2.4 Hidden symmetry and topological classification

In addition to the pairing of zero modes at opposite wavenumber, they must also appear in complex-conjugate pairs since these wavenumbers are the roots of the determinant of the compatibility matrix. These two facts imply that for a real-valued wavenumber in one direction there are zero modes whose wavenumbers in the transverse direction have imaginary parts that are equal and opposite. Zero modes with complex-valued wavevectors is a hallmark of topological polarization and this feature explains the absence of such topological polarization observed in Maxwell origami [86].

The determinant of the compatibility matrix is generically a Laurent polynomial in the Bloch factors

$$\det \mathbf{C}(\mathbf{q}) = \sum_{m,n} c_{mn} z_1^m z_2^n, \tag{3.28}$$

that vanishes for wavevectors at which zero modes exist and the integers m, n are bound by the total number of edges connecting the unit cell to adjacent cells. Roots of such polynomials generically arise in complex-conjugate pairs (in the Bloch factors) where the complex part of the wavenumber, $k^\mu = \mathrm{Im} q^\mu$, specifies the inverse decay length of the mode. Hence, for every mode at z_1, z_2 there is a mode at z_1^*, z_2^* and equivalently, for every mode at $\mathbf{q}$, there is a mode at $-\mathbf{q}^*$. Thus, by the hidden symmetry pairing modes at $\mathbf{q}$ and $-\mathbf{q}$, there is also a mode at $\mathbf{q}^*$ so that for every mode exponentially localized on one side of the sheet there is another mode exponentially localized to the opposite side as shown in Figure 3.4.

As discussed in subsection 2.2.2, for generic compatibility matrices (such as the rigidity matrix for frames), the existence of exponentially localized modes indicated by finite-valued inverse decay rates is topologically protected by the winding number [79]. This quantity is obtained by integrating the phase of the compatibility matrix over a direction in the Brillouin zone. However, since Maxwell origami has such exponentially localized

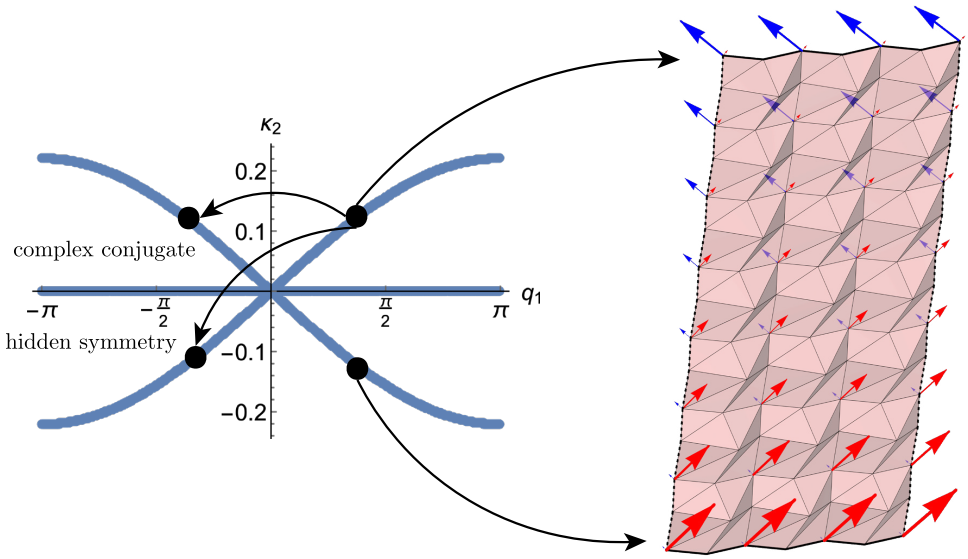

Figure 3.4: Zero modes generically arise at complex wavenumber, q, whose imaginary part, k, specifies the inverse decay rate of the mode. These always arise in complex conjugates $\mathbf{q}$ and $-\mathbf{q}^*$ while for Maxwell origami the hidden symmetry implies they also arise in pairs $\mathbf{q}$ and $-\mathbf{q}$. Together, these facts imply zero modes are paired at $\mathbf{q}$ and $\mathbf{q}^*$, so that exponentially localized edges modes arise in pairs and Maxwell origami cannot be topologically polarized.

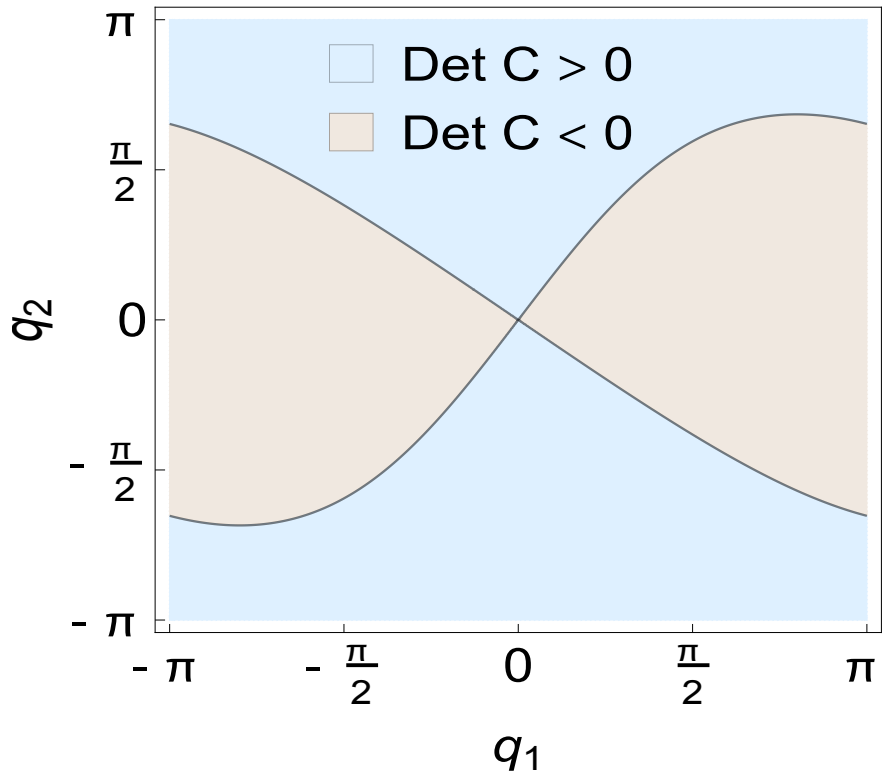

Figure 3.5: The hidden symmetry of Maxwell origami implies the determinant of its compatibility matrix is real-valued over the Brillouin zone indicating that its winding number always vanishing and that it belongs to a unique topological class.

modes arise in pairs on opposite edges this winding number always vanishes, indicating that the determinant of the compatibility matrix is real-valued as shown in Figure 3.5. Such real-valued compatibility matrices fall in the special topological class predicted by Roychowdhury and Lawler [88] that also includes spin magnets [89] as well as systems with contrived symmetries [99]. I discuss future work towards understanding and utilizing these unique topological properties in section 3.5.

3.3 Second-order conditions and branching

In order for first-order folding motions to generate the space of rigidly foldable configurations there must exist second-order folding motions that ensure the vertex compatibility condition is satisfied to second order as discussed in subsection 2.1.2. The existence of

such second-order folding motions is characterized by a quadratic condition on the first-order folding motions that branches the configuration space from the spatially-periodic state into two two-dimensional surfaces distinguished by whether configurations fold upwards or downwards into a cylinder. While less intuitive than the linear vertex compatibility condition, this quadratic compatibility condition relates the angular velocity generated by second-order folding motions on the creases with the angular velocity generated by first-order folding motions on the rotated creases, where this rotation is itself a function of the first-order folding motions, similar to the condition for the second-order rigidity of frames [68].

3.3.1 Second-order folding motions

Consider an infinitesimal change to the fold angles denoted by $\rho_{(i,j)} \rightarrow \rho_{(i,j)} + \epsilon\phi_{(i,j)} + \epsilon^2\psi_{(i,j)}$ where $\phi_{(i,j)}$ satisfies the linear vertex compatibility condition in Equation 3.14. The corresponding expansion of the vertex compatibility condition in Equation 3.6 to second order in ϵ^2 contains terms linear in $\psi_{(i,j)}$ and terms quadratic in $\phi_{(i,j)}$. While the former terms are equivalent to those in Equation 3.14 with the exchange of first-order folding motions for second-order folding motions, the latter are non-trivial combinations of the generators of rotation

$$\sum_{j'} \boldsymbol{\sigma}^{(1)}_{(i,j')}\psi_{(i,j')} + \sum_{j',k'>j'} \phi_{(i,j')}\phi_{(i,k')}\boldsymbol{\sigma}^{(1)}_{(i,j')}\boldsymbol{\sigma}^{(1)}_{(i,k')} + \frac{1}{2}\sum_{j'} \phi^2_{(i,j')}\boldsymbol{\sigma}^{(2)}_{(i,j')} = \mathbf{0}, \tag{3.29}$$

$$\boldsymbol{\sigma}^{(2)}_{\hat{x}} = \begin{pmatrix} 0 & 0 & 0 \\ 0 & -1 & 0 \\ 0 & 0 & -1 \end{pmatrix}, \tag{3.30}$$

where the superscript distinguishing between the first-order and second-order generators of rotation (obtained by Taylor-expanding a rotation matrix about a rotation angle of zero) and

they are defined about the (i,j) edges due to the similarity transformations in Equation 3.1. Since the first-order generator is skew-symmetric, the diagonal components of the terms quadratic in the first-order folding motions must vanish.

Such diagonal components can be rewritten in index notation

$$\left(\boldsymbol{\sigma}^{(1)}_{(i,j)}\boldsymbol{\sigma}^{(1)}_{(i,k)}\right)^{\alpha\beta} = \hat{r}^{\alpha}_{(i,j)}\hat{r}^{\beta}_{(i,k)} - \hat{r}_{(i,j)}\cdot\hat{r}_{(i,k)}\delta^{\alpha\beta}, \tag{3.31}$$

where $\delta^{\alpha\beta}$ is the Kronecker-delta function. Hence, the sum in Equation 3.29 over $k' > j'$ is related to the two independent sums that each vanish for first-order folding motions

$$\begin{aligned}\sum_{j',k'}\phi_{(i,j')}\phi_{(i,k')}\left(\hat{r}^{\alpha}_{(i,j)}\hat{r}^{\beta}_{(i,k)} - \hat{r}_{(i,j)}\cdot\hat{r}_{(i,k)}\delta^{\alpha\beta}\right) &= 2\sum_{j',k'>j'}\phi_{(i,j')}\phi_{(i,k')}\left(\hat{r}^{\alpha}_{(i,j)}\hat{r}^{\beta}_{(i,k)} - \hat{r}_{(i,j)}\cdot\hat{r}_{(i,k)}\delta^{\alpha\beta}\right)\\ &\quad + \sum_{i,j'}\phi^{2}_{(i,j')}\left(\hat{r}^{\alpha}_{(i,j')}\hat{r}^{\beta}_{(i,j')} - \delta^{\alpha\beta}\right) = \mathbf{0}.\end{aligned} \tag{3.32}$$

Thus, the diagonal components of the sum over $k' > j'$ exactly cancel the sum over $\phi^{2}_{(i,j')}$ and Equation 3.29 is a skew-symmetric matrix condition.

The remaining off-diagonal terms are equivalent to the sum over cross products of the edges, which take a form reminiscent of the formula for vertex displacements in Equation 3.25 by appropriate use of parenthesis

$$\sum_{j',k'>j'}\phi_{(i,j')}\phi_{(i,k')}\boldsymbol{\sigma}^{(1)}_{(i,j')}\boldsymbol{\sigma}^{(1)}_{(i,k')} = \sum_{j'}\phi_{(i,j')}\Big(\sum_{k'>j'}\phi_{(i,k')}\hat{r}_{(i,k')}\Big)\times\hat{r}_{(i,j')}, \tag{3.33}$$

with the distinction that the angular velocity defined by the interior sum is in respect to a different starting point at each vertex. However, since the first-order folding motions satisfy the linear compatibility condition, any constant rotation, $\boldsymbol{\omega}_{(i,j,k)} - \boldsymbol{\omega}_{(i_0,j_0,k_0)}$, vanishes in the sum over j'. Thus, these cross products indeed correspond to the amount each edge

direction is rotated, $\dot{\hat{r}}_{(i,j')}$, and the quadratic vertex compatibility condition is given by the vector equation

$$\sum_{j'} \psi_{(i,j')} \hat{r}_{(i,j')} + \sum_{j'} \phi_{(i,j')} \dot{\hat{r}}_{(i,j')} = \mathbf{0}. \tag{3.34}$$

Similar to the linear compatibility conditions, this can be written by defining a quadratic compatibility matrix $\dot{\mathbf{C}}(\boldsymbol{\phi})$ that is a function of the first-order folding motions to yield

$$\mathbf{C}\boldsymbol{\psi} + \dot{\mathbf{C}}(\boldsymbol{\phi})\boldsymbol{\phi} = \mathbf{0}. \tag{3.35}$$

Moreover, the primary interest is to determine under what conditions do second-order folding motions exist rather than to determine the second-order folding motions explicitly. Such conditions are shown in subsection 3.3.2 to be given by a homogeneous quadratic polynomial in coefficients of the first-order folding motions, thereby distinguishing branches of solutions due to the two roots of any quadratic.

3.3.2 Configuration space branching

The pairing of rigid body modes and uniform, first-order folding motions in subsection 3.2.2 yields a different number of first-order folding motions in spatially periodic (three modes) and screw-periodic (two modes) configurations. This suggests that the three first-order folding motions in the spatially periodic state do not generically admit second-order folding motions to rigidly fold the origami sheet. Indeed, the quadratic compatibility condition in Equation 3.35 only admits solutions to the second-order folding motions if the first-order folding motions transform the spatially-periodic sheet in a screw-periodic manner. While the analysis of subsection 3.1.2 indicates this is certainly a necessary condition, it is also a sufficient condition because the left and right null spaces of the compatibility matrix for Maxwell origami must have the same dimension.

Suppose indeed that the first-order folding motion, written as a linear combination of

the three modes from the spatially periodic state, $\boldsymbol{\phi} = \sum_\mu \lambda_\mu \boldsymbol{\phi}_\mu$, rotates the edges in a cylindrically symmetric manner. Then the infinitesimally deformed compatibility matrix, $\mathbf{C} + \dot{\mathbf{C}}(\boldsymbol{\phi})$ exhibits a two-dimensional left null space spanned by the two cylindrical symmetries. Let such a rigid body mode be written as a linear combination of the spatially-periodic rigid body modes and some infinitesimal change $\mathbf{u} + \delta\mathbf{u}$. Hence, the transpose of the compatibility matrix satisfies

$$\big(\mathbf{C} + \dot{\mathbf{C}}(\boldsymbol{\phi})\big)^T(\mathbf{u} + \delta\mathbf{u}) = O(\epsilon^3), \tag{3.36}$$

so that by the mechanical criticality of Maxwell origami there must exist some second-order folding motion satisfying

$$\big(\mathbf{C} + \dot{\mathbf{C}}(\boldsymbol{\phi})\big)(\boldsymbol{\phi} + \boldsymbol{\psi}) = O(\epsilon^3), \tag{3.37}$$

showing that the requirement for the first-order folding motions to induce cylindrically symmetric rotations of the edges is sufficient for the existence of second-order folding motions.

It is more practical to note that projecting the three rigid body modes from the left onto the quadratic compatibility condition in Equation 3.35 yields three independent sums over each quadratic vertex compatibility condition in Equation 3.34. Naturally, the terms linear in the second-order folding motions vanish because the rigid body modes are in the left null space of the compatibility matrix. In contrast, this projection sums the terms quadratic in the first-order folding motions at each vertex i. Since any constant angular velocity can be added to these terms, their summation effectively gives the intercellular orientation compatibility condition

$$\sum_{i,(i,j'),(i,k')} \phi_{(i,j')}\phi_{(i,k')}\hat{r}_{(i,j')} \times \hat{r}_{(i,k')} = \boldsymbol{\Omega}_1 \times \boldsymbol{\Omega}_2 = \mathbf{0}. \tag{3.38}$$

Moreover, because intercellular position compatibility ensures that these lattice angular

velocities are co-planar, this yields a single constraint on the first-order folding motion coefficients, thus explaining the contraction from an apparent three-dimensional space of first-order folding motions to a two-dimensional surface of rigidly foldable cylindrical configurations. This branching is the periodic equivalent to that for developable vertices explored by Chen and Santangelo [94]. In contrast, since the first-order folding motions from a screw-periodic configuration retain the screw periodicity, they generically extend to second order.

3.4 Numerical confirmation of degenerate ground states

In this chapter, I have made analytical arguments in support of the argument by Tachi [91] for Maxwell origami to have a two-dimensional space of rigidly foldable cylindrical configurations. Additionally, I have shown the existence of an additional first-order folding motion in spatially-periodic configurations that leads to branching of the configuration space due to the sheet folding upwards or downwards into a cylinder. Here, I verify the existence of this two-dimensional configuration space numerically by considering the simplest, nontrivial Maxwell origami unit cell: eight triangular faces.

I initialize such an origami sheet in a spatially-periodic configuration with arbitrarily chosen sector and fold angles so that the vertices are not co-planar. I construct the compatibility matrix defined by Equation 3.14 and numerically determine its null space, which is indeed three dimensional. Then, I use the intercellular orientation compatibility condition to determine which linear combinations of these first-order folding motions induce cylindrically symmetric rotations of the edges. Finally, I evolve the sheet along such directions by stepping in the direction of a first-order folding motion and minimizing an energy functional defined by violations of the vertex compatibility condition in Equation 3.6.

This sequence provides trajectories of fold angles for rigidly foldable configurations that I then map to vertex positions, lattice vectors, and lattice rotations to reconstruct the origami sheet at each step. Since the configuration space is twelve-dimensional (due to

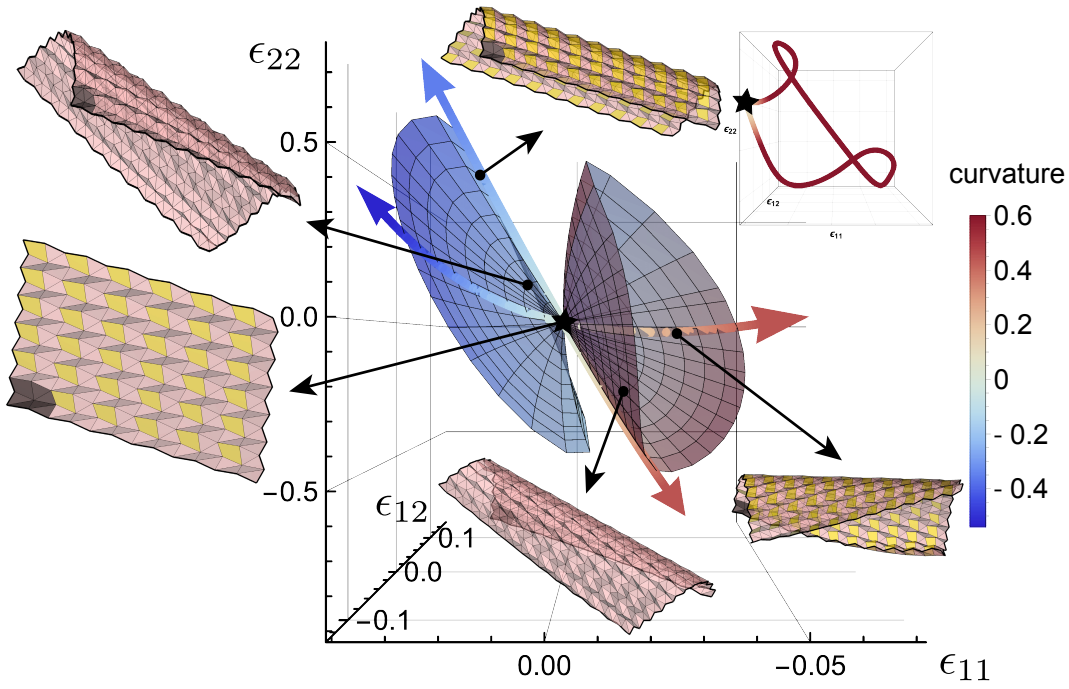

Figure 3.6: The two-dimensional space of rigidly foldable cylindrical configurations for generic Maxwell origami projected onto the space of lattice vector strains. The color bar indicates the radius of the cylindrical curvature where blue (red) correspond to downward folded and upward folded cylindrical configurations that branch from the spatially periodic configuration. The black arrows show the spatial embedding of the corresponding point in configuration space and the one-dimensional lines through configuration space are obtained by constraining two adjacent triangular faces (indicated by the yellow quadrilaterals) to fuse together.

the twelve creases in the unit cell), I project each state into the three-dimensional space of strains of the lattice vectors as shown in Figure 3.6..

3.5 Discussion

I have explored periodic origami sheets composed entirely of triangular faces called Maxwell origami. I derived compatibility conditions on these sheets at first, second, and infinite order. I showed that a hidden symmetry between the first-order folding motions pairs linear zero modes at opposite wavenumber and explored the consequences for uniform and nonuniform modes. For uniform modes, this hidden symmetry implies the existence of a two-dimensional space of degenerate ground states, where the sheet forms a section of a

cylinder, that bifurcates from the spatially-periodic configuration due to symmetry breaking. For nonuniform modes, this hidden symmetry implies that exponentially localized edge modes come in pairs on opposite sides of the sheet indicating that Maxwell origami belongs to the topological class of materials with real-valued compatibility matrices.

The importance of this chapter is that triangulations have been shown to capture the mechanical response of most crease patterns, even those with non-triangular faces. Thus, the results for Maxwell origami serve as a foundation for all periodic crease patterns. In particular, the topological classification of Maxwell origami warrants further investigation to permit the robustness of topologically protected modes in the design of origami structures. This topological class exhibits Z_2 invariants indicating modes could be exponentially localized between the two phases as shown for a modified SSH model of the same topological class [99]. Since this class is largely unexplored, Maxwell origami serves as an experimental model to understand to test and understand features of the class so that they may be applied to similar systems when they are discovered.

CHAPTER 4

DISCRETE SYMMETRIES AND THE FOUR-PARALLELOGRAM ORIGAMI

The analysis of Maxwell origami in chapter 3 implies that because every quadrilateral face can be treated as two triangular faces with an additional constraint, crease patterns with two or more quadrilateral faces are generically rigid. However, as discussed in subsection 2.1.4, discrete symmetries can render these constraints redundant. Indeed, a number of quadrilateral-based crease patterns are known to rigidly fold [100, 101, 60, 102], with several exhibiting negative Poisson ratios [2, 61, 5, 6]. Here, I show that these negative Poisson ratio crease patterns belong to a broader family whose discrete symmetry divides the linear compatibility matrix into symmetric and antisymmetric sectors with opposite generalized Poisson ratios, thereby ensuring there is always one auxetic mode.

In contrast to triangulations, quadrilateral-based origami crease patterns admit linear isometries that bend faces, as can be captured by the triangulation of the quadrilateral faces [3, 13]. This means such crease patterns always exhibit three linear isometries, independent of any discrete symmetries, per the analysis of chapter 3. Unfortunately, triangulating these faces makes it difficult to determine and understand the role of such symmetries.

I address this issue by reformulating the compatibility conditions of chapter 3 so that the linear isometries are described by scalar amplitudes on the vertices and faces. This reveals an explicit permutation symmetry, or more specifically an antisymmetry, that characterizes the linear compatibility matrix. As such, this matrix is divided into symmetric and antisymmetric sectors of modes that have distinct properties. Indeed, I show that the symmetry of the mode determines its ability to generate strain or curvature: symmetric modes exhibit purely in-plane strain while antisymmetric modes exhibit purely out-of-plane curvature. Moreover, these deformations define in-plane and out-of-plane generalized *lattice* Poisson ratios which are always equal and opposite, thereby generalizing the result of previous

studies.

This chapter is based on a manuscript being prepared for submission as I write this thesis and is organized as follows. In section 4.1, I present the four-parallelogram origami family and parameterize its one-dimensional configuration space. In section 4.2, I construct compatibility conditions on the linear deformations of parallelogram-based origami and express these modes via eigenstates of the permutation symmetry in the four-parallelogram family. In section 4.3, I map these modes to intercellular strains and curvatures to show that the symmetric and antisymmetric eigenstates generate distinct mechanical responses, emphasizing they have equal and opposite lattice Poisson ratios. In section 4.4, I summarize this work and discuss potential for future investigations.

4.1 The four-parallelogram origami

While periodic origami with two or more quadrilateral faces is generically rigid per the analysis of chapter 3, members of the four-parallelogram origami are known to rigidly fold. Such rigid foldability arises from a degeneracy in the constraints due to the symmetry of the vertices so that its configuration space is described by the rigid embeddings of a single four-coordinated vertex [60]. Here, I introduce the four-parallelogram family of origami crease patterns and parameterize their one-dimensional space of degenerate ground states.

Consider the four-parallelogram origami shown in Figure 4.1. The unit cell is composed of four generic parallelogram faces, each with a sector angle α_A in non-adjacent corners and its supplement, $\pi - \alpha_A$, in adjacent corners. These faces share non-adjacent creases with the same partner where the dihedral angles (the complement of the fold angle from chapter 3, used here for the upcoming application of spherical trigonometry) are complements of one another, $\gamma^A_{i+2} = 2\pi - \gamma^A_i$, so that the sheet is spatially periodic. Lastly, in contrast to triangular faces where the interior angles determine the edge lengths, there are four unique edge lengths required to parameterize the four-parallelogram origami denoted by r_i.

Pairs of non-adjacent edges define the lattice vectors $\boldsymbol{\ell}_1 = \mathbf{r}_1 + \mathbf{r}_3$, $\boldsymbol{\ell}_2 = \mathbf{r}_2 + \mathbf{r}_4$ which

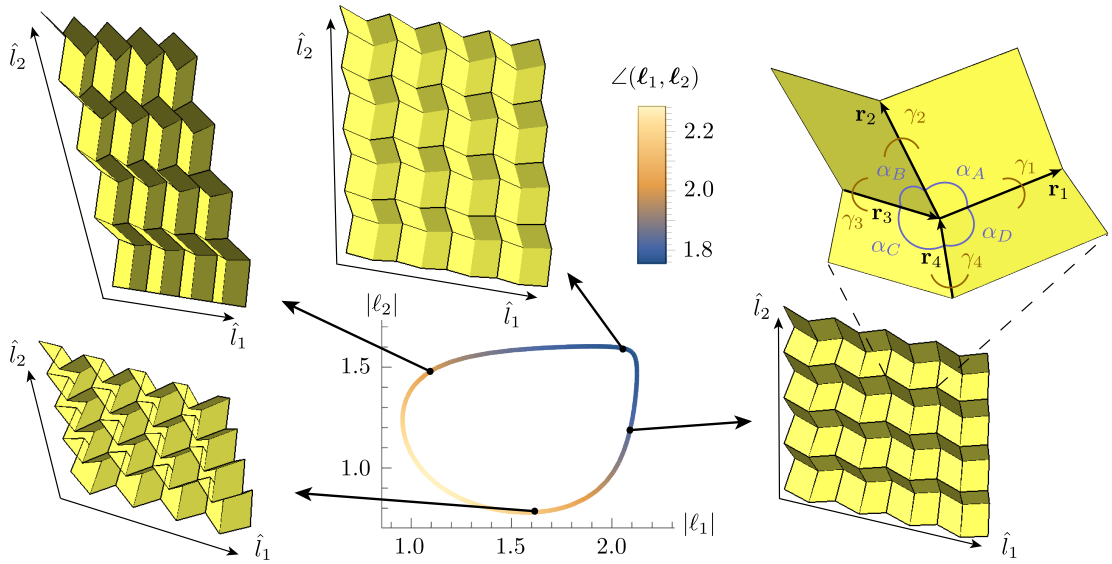

Figure 4.1: The four-parallelogram origami is a spatially-periodic origami sheet composed of unit cells with four parallelogram faces. The sector angles of a face are identical, α_A, in non-adjacent corners and supplementary, $\pi - \alpha_A$, in adjacent corners. The dihedral angles are complementary on parallel edges, $\gamma^A_{i+2} = 2\pi - \gamma^A_i$, to enforce spatial periodicity. The four unique edge directions, denoted $\mathbf{r}_i$, specify the two lattice vectors $\boldsymbol{\ell}_1 = \mathbf{r}_1 + \mathbf{r}_3, \boldsymbol{\ell}_2 = \mathbf{r}_2 + \mathbf{r}_4$ which are generically not orthogonal and the angle between them varies as the sheet rigidly folds along its one-dimensional configuration space.

are not necessarily orthogonal to one another. However, the subspace of orthotropic four-parallelogram origami is obtained by enforcing the one-dimensional constraint

$$\boldsymbol{\ell}_1 \cdot \boldsymbol{\ell}_2 = r_1 r_2 \cos\alpha_A - r_2 r_3 \cos\alpha_B + r_3 r_4 \cos\alpha_C - r_4 r_1 \cos\alpha_D = 0, \tag{4.1}$$

that importantly depends only on the static edge lengths and sector angles. Similarly, the subspace of developable crease patterns is obtained by enforcing the one-dimensional constraint on the sector angles

$$\alpha_A + \alpha_B + \alpha_C + \alpha_D = 2\pi. \tag{4.2}$$

Lastly, the orthotropic family of Morph patterns is obtained by requiring $\alpha_A = \alpha_B$ and $\alpha_C = \alpha_D$, which itself reduces to the developable Miura-ori for $\alpha_C = 2\pi - \alpha_A$ and the eggbox $\alpha_C = \alpha_A$. All of these crease patterns exhibit a one-dimensional space of rigidly foldable, spatially-periodic configurations.

The rigid foldability of the four-parallelogram origami arises due to a degeneracy in the constraints that, for origami composed of four generic quadrilateral faces, would otherwise render the sheet rigid due to the analysis of chapter 3. Since each vertex has the same, up to the supplement, sector angles and the same, up to the complement, dihedral angles the solutions to the rigid embeddings at each vertex are mutually compatible. This indicates the existence of a rigid mode comprised entirely of vertex folding. Moreover, this vertex folding exhibits an explicit parameterization via spherical trigonometry, an equivalent but more accessible constraint than the vertex compatibility condition Equation 3.6.

The directions of edges at an origami vertex project onto the unit sphere defining a spherical quadrilateral whose interior angles are the dihedral angles and edges are great circles subtending the corresponding sector angle as shown in Figure 4.2(a). A fifth great circle segment can be used to triangulate the quadrilateral by connecting the corners with interior angles either γ_1 and γ_3 or γ_2 and γ_4. Without loss of generality, let γ_{24} be the fifth

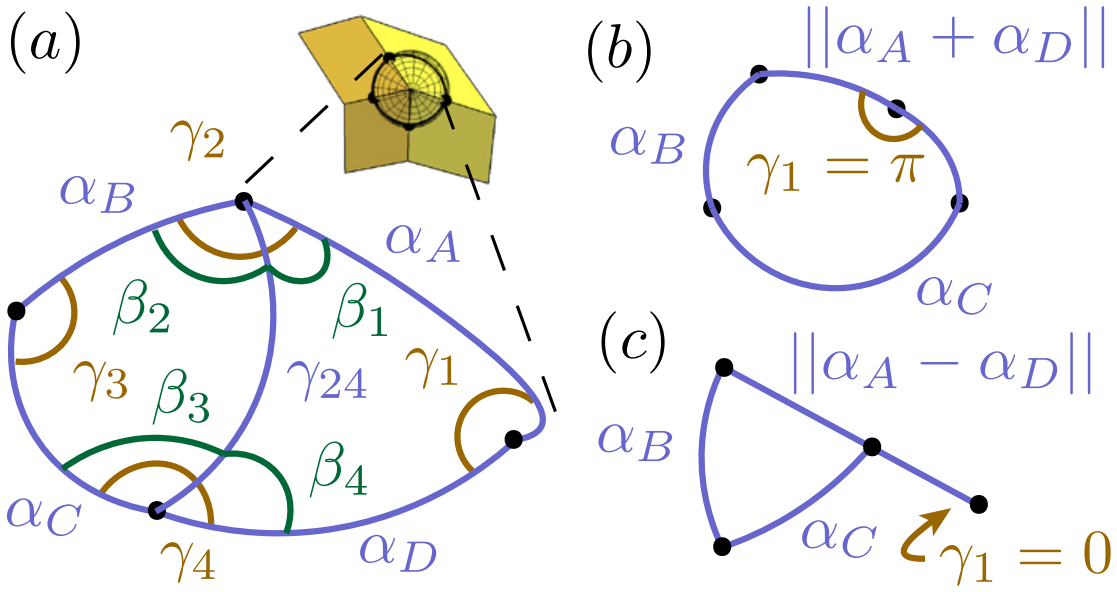

Figure 4.2: (a) The embedding of a four-coordinated vertex projects onto the embedding of a spherical quadrilateral whose sides are given by segments of great circles with angular length corresponding to the sector angles, α_A, of the vertex and whose interior angles are given by the dihedral angles of the edges. This spherical quadrilateral can be triangulated by introducing a fifth great circle that divides the two interior angles, $\gamma_2 = \beta_1 + \beta_2$, $\gamma_2 = \beta_3 + \beta_4$, so that the dihedral angles can be parameterized using spherical trigonometry. Depending on the assignment of sector angles, different sides of these spherical quadrilaterals are able to fully open (b) and fully close (c), thereby distinguishing connected and disconnected configuration spaces.

great circle segment that divides γ_2 and γ_4 and denote the interior angles summing to the divided dihedral angles as $\gamma_2 = \beta_1 + \beta_2$, $\gamma_2 = \beta_3 + \beta_4$. The spherical laws of sine and cosine relate these angles

$$\cos\gamma_{24} = \cos\alpha_A\cos\alpha_D + \sin\alpha_A\sin\alpha_D\cos\gamma_1 = \cos\alpha_B\cos\alpha_C + \sin\alpha_B\sin\alpha_C\cos\gamma_3,$$
$$\cos\beta_2 = \frac{\cos\alpha_D - \cos\gamma_{24}\cos\alpha_A}{\sin\gamma_{24}\sin\alpha_A}, \qquad \cos\beta_4 = \frac{\cos\alpha_A - \cos\gamma_{24}\cos\alpha_D}{\sin\gamma_{24}\sin\alpha_D},$$
$$\cos\beta_1 = \frac{\cos\alpha_C - \cos\gamma_{24}\cos\alpha_B}{\sin\gamma_{24}\sin\alpha_C}, \qquad \cos\beta_4 = \frac{\cos\alpha_B - \cos\gamma_{24}\cos\alpha_C}{\sin\gamma_{24}\sin\alpha_B}, \tag{4.3}$$

$$\frac{\sin\gamma_1}{\sin\gamma_{24}} = \frac{\sin\beta_1}{\sin\alpha_D} = \frac{\sin\beta_4}{\sin\alpha_A}, \qquad \frac{\sin\gamma_3}{\sin\gamma_{24}} = \frac{\sin\beta_2}{\sin\alpha_C} = \frac{\sin\beta_3}{\sin\alpha_B}. \tag{4.4}$$

This permits the parameterization of γ_3 in terms of γ_1 or vice versa, noting there are always two solutions because $\arccos$ is multivalued over the unit circle. This choice determines the diagonal, γ_{24}, which can then be used to compute the remaining interior angles β_i and sum them for the last two dihedral angles γ_2, γ_4. The $\arctan$ function determines the exact quadrant these solutions lie in

$$\gamma_2 = \arctan\frac{\sin\gamma_1\sin\alpha_D\sin\alpha_A}{\cos\alpha_D - \cos\gamma_{24}\cos\alpha_A} + \arctan\frac{\sin\gamma_1\sin\alpha_A\sin\alpha_D}{\cos\alpha_A - \cos\gamma_{24}\cos\alpha_D} \tag{4.5}$$

$$\gamma_4 = \arctan\frac{\sin\gamma_3\sin\alpha_C\sin\alpha_B}{\cos\alpha_C - \cos\gamma_{24}\cos\alpha_B} + \arctan\frac{\sin\gamma_3\sin\alpha_B\sin\alpha_C}{\cos\alpha_B - \cos\gamma_{24}\cos\alpha_C}. \tag{4.6}$$

The key to the four-parallelogram origami is that adjacent vertices have supplementary sector angles: applying this to the above solutions indeed reveals that when the dihedral angles on shared edges are identical, the dihedral angles on parallel edges are complementary, thereby permitting rigid folding through spatially-periodic configurations.

In principle the choice to complete this parameterization by varying γ_1 or γ_3 is trivial however, their domains are generically distinct. Indeed, the domain of $\arccos$ constrains

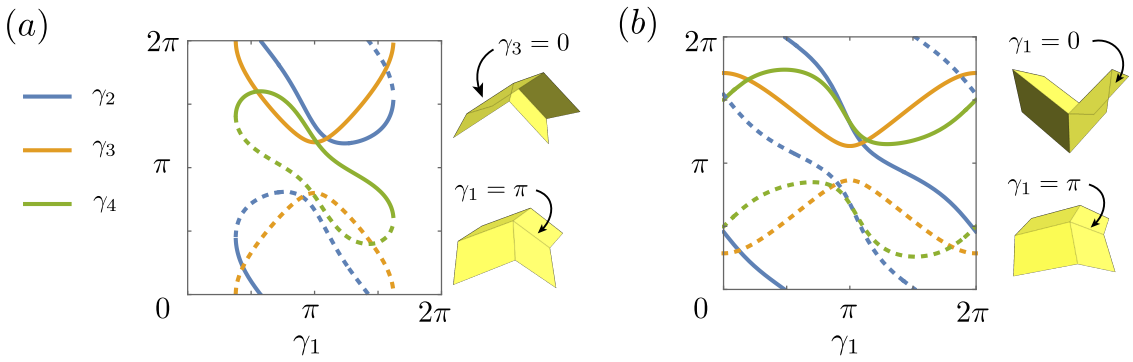

Figure 4.3: The configuration space of the four-parallelogram origami is completely determined by that of one of its vertices. Such four-coordinated vertices have a one-dimensional space of degenerate ground states, though depending on the sector angles this space map be (a) connected or (b) disconnected.

the dihedral angles that yield real-valued diagonal

$$\gamma_1 = 0 \implies \gamma_{24} = \arccos\Big(\cos\alpha_A \cos\alpha_D + \sin\alpha_A \sin\alpha_D\Big), \tag{4.7}$$

$$\gamma_1 = \pi \implies \gamma_{24} = \arccos\Big(\cos\alpha_A \cos\alpha_D - \sin\alpha_A \sin\alpha_D\Big). \tag{4.8}$$

The same must hold for γ_3 replacing $\alpha_A \to \alpha_B$ and $\alpha_D \to \alpha_C$ though γ_{24} is only real-valued provided the arguments are over the interval $[0, 1]$ implying one edge may open or close while the other may be locked from doing so. Thus, the diagonal is bounded

$$\gamma_{24,\text{min}} = \max\Big(|\alpha_A - \alpha_D|, |\alpha_B - \alpha_C|\Big), \qquad \gamma_{24,\text{max}} = \min\Big(|\alpha_A + \alpha_D|, |\alpha_B + \alpha_C|\Big), \tag{4.9}$$

where the inner product $|x| = \min(x, 2\pi - x)$ is the geodesic length of the corresponding great circle taking x to always be positive valued. Hence, there are two distinct cases: the same sector angle pair determines both bounds or each sector angle pair determines a single bound. In the former this corresponding dihedral angle's domain contains both the opened state π and the closed state 0 (and hence also 2π implying the configuration space

is a non-contractible loop. Moreover, since the constraints are multi-valued this implies the two solutions form two independent loops as shown in Figure 4.3(b). On the other hand if each dihedral angle's domain only contains 0 or π then these two solutions join to form a single contractible loop in the configuration space as shown in Figure 4.3(a).

4.2 Isometric linear modes

The isostaticity of triangular faces means that gradients in the anglular velocity defined by Equation 3.24 only arise between crease-sharing faces. However, non-triangular faces, in particular parallelograms, have linear isometries that include bending of the faces so that the angular velocity field may vary across a face as well. Here, I derive the resulting linear compatibility condition in origami composed of parallelogram faces in subsection 4.2.1 and determine the modes for the particular case of the *four-parallelogram* origami, where symmetries play a vital role in the characterization of the modes, in subsection 4.2.2.

4.2.1 Compatibility in generic parallelogram-based origami

The linear isometries of parallelogram-based origami are composed of crease folding (similar to that of the triangulations in chapter 3) as well as face bending. This deformations are quantified by an angular velocity field that now varies across the sheet under the compatibility condition that elements of the sheet are not rotated relative to themselves. Locally, the crease folding and face bending exhibit exact solutions up to overall amplitudes located on the vertices and faces. These amplitudes are constrained by edge compatibility conditions that can be combined to define a square compatibility matrix whose null space spans the isometric linear modes.

The angular velocity field, $\boldsymbol{\omega}$, rotates elements of the sheet, $d\mathbf{s} \to d\mathbf{s} + \boldsymbol{\omega} \times d\mathbf{s}$, provided elements do not rotate relative to themselves as specified by the condition

$$\oint \boldsymbol{\omega} \times d\mathbf{s} = \mathbf{0}, \tag{4.10}$$

where the integral is taken over any closed loop along the surface of the sheet such as that shown in Figure 4.4(a). Since the surface elements lie within the plane of particular faces, the angular velocity field cannot exhibit any gradients normal to this plane. Moreover, because every crease is shared by two faces the angular velocity gradients must lie in both planes simultaneously, hence these gradients are proportional to the edges themselves. The distinction from triangulations is that now the angular velocity can change on a path *along* an edge, in addition to across an edge, thereby generating rotations between corners of a face.

Thus, the angular velocity gradients are comprised of two components. The first, analogous to the first-order folding motions of triangulations, is due to folding in the vicinity of a particular vertex denoted by $\pm\phi_i^a$. The second is due to bending of a particular face characterized by the *torsion* applied to the normal vector of the face denoted by $\pm\tau_i^A$. Here, I use the local basis defined in Figure 4.4(b) and Figure 4.4(c) where the lowercase (uppercase) superscripts specify the vertex (face), the subscript denotes the locally defined edge, denoted by $\mathbf{v}_i^a$ ($\mathbf{v}_i^A$) in counterclockwise order around the vertex (face), and the sign is positive or negative depending if the edge is crossed in a counterclockwise or clockwise manner around the vertex (face).

As before, these angular velocity gradients accumulate across the sheet

$$\boldsymbol{\omega}^{a,A} - \boldsymbol{\omega}^{a_0,A_0} = \sum \pm\phi_{i'}^{a'}\hat{v}_{i'}^{a'} + \sum \pm\tau_{i'}^{A'}\hat{v}_{i'}^{A'}, \tag{4.11}$$

where the paired superscript (a, A) specifies the corner of face A that contains vertex a and the sum is taken over all edges crossed and traversed. These angular velocity gradients rotate elements of the sheet, thereby generating vertex displacements

$$\mathbf{u}^{a,A} - \mathbf{u}^{a_0,A_0} = \sum \left(\boldsymbol{\omega}^{a',A'} - \boldsymbol{\omega}^{a_0,A_0}\right) \times \mathbf{v}_{i'}^{a'}, \tag{4.12}$$

where the face dependence of the displacements can lead to global rotations of the sheet.

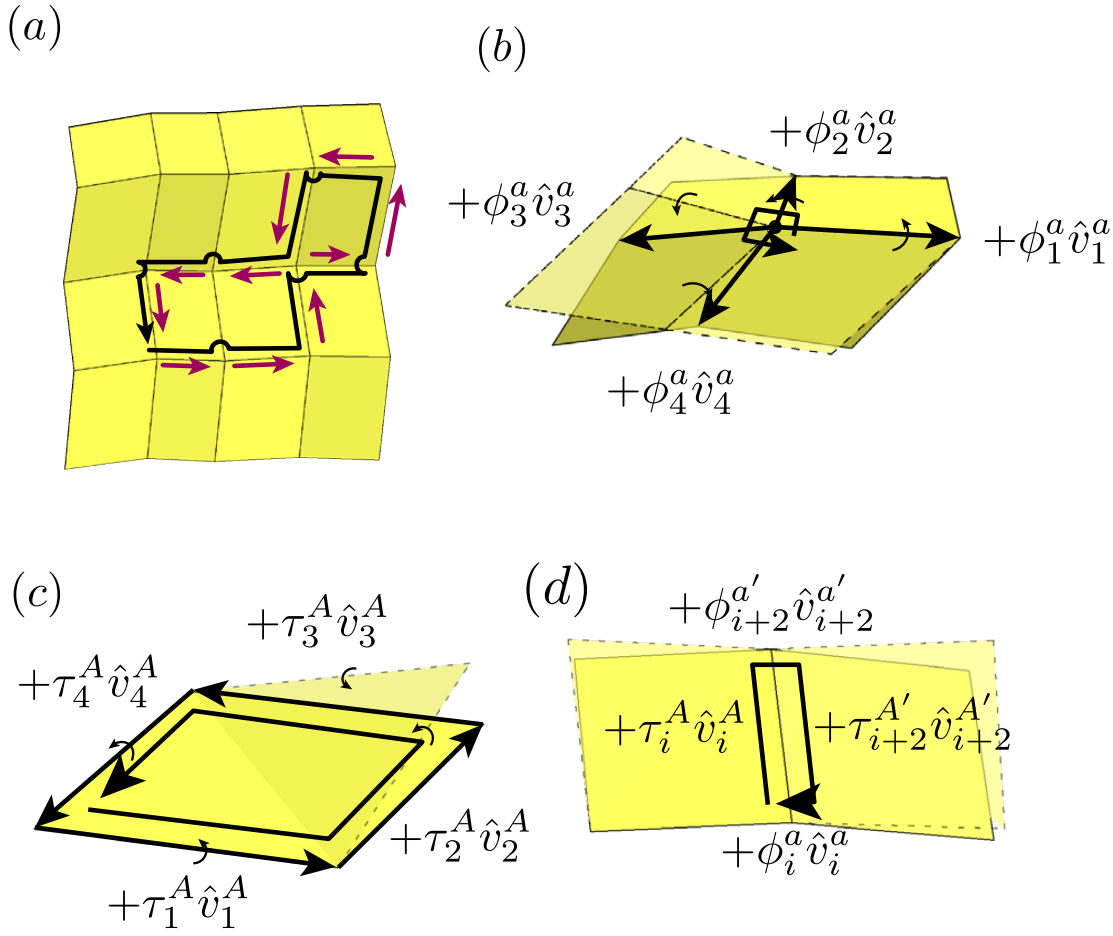

Figure 4.4: (a) The angular velocity field, $\boldsymbol{\omega}$, must vanish around closed loops, such as that indicated by the black arrows. This field rotates elements of the sheet, $d\mathbf{s} \rightarrow d\mathbf{s}\boldsymbol{\omega} \times d\mathbf{s}$, such as those indicated by the maroon arrows provided that these rotations are compatible. (b) Edges are locally defined in the vicinity of vertex a as $\mathbf{v}_i^a$ where the subscript increases on a path counterclockwise around the vertex. Vertex folding is represented by a local assignment of first-order folding motions, ϕ_i^a, that are subject to the orientation compatibility condition in Equation 4.13. (c) Edges are locally defined on a face A by $\mathbf{v}_i^A$ where the subscript i increases on a path counterclockwise around the face. Face bending is represented by a torsion, τ_i^A, applied to the face that is subject to the orientation and position compatibility conditions in Equation 4.16 and Equation 4.17 respectively. (d) The closed paths around edges constrain the locally defined vertex folding and face bending via orientation compatibility in Equation 4.19, thereby defining the linear compatibility matrix.

The vertex folding and face torsions describe isometric linear modes when both the angular velocity gradients in Equation 4.11 and the vertex displacements in Equation 4.12 vanish along closed paths. Such paths are composed of individual loops around vertices and faces, yielding local compatibility conditions, along with loops around edges that couple the local solutions to constrain global solutions.

Since vertices are zero-dimensional points, a path around a vertex cannot result in any displacement and the local compatibility condition is analogous to Equation 3.14 with the caveat it only holds in the immediate vicinity of the vertex

$$\sum \phi_{i'}^{a'} \hat{v}_{i'}^{a'} = \mathbf{0}. \tag{4.13}$$

Since every vertex is four-coordinated in parallelogram-based origami, this condition admits a one-dimensional family of solutions provided the constraints are non-degenerate. Such solutions are generically determined by projecting the condition onto the cross product of any two local edge directions, thereby coupling the amount of folding on the two remaining edges

$$\zeta_i^a \equiv \hat{v}_{i+1}^a \cdot \hat{v}_{i+2}^a \times \hat{v}_{i+3}^a, \tag{4.14}$$

$$\phi_i^a = (-1)^i \mathcal{V}^a \zeta_i^a, \tag{4.15}$$

where the triple products ζ_i^a are called the folding coefficients and the scalar $\mathcal{V}$ is called the vertex amplitude.

In contrast, faces are two-dimensional so that face bending induces some amount of displacement between non-adjacent vertices in addition to rotation

$$\sum \tau_{i'}^{A} \hat{v}_{i'}^{A} = \mathbf{0}, \tag{4.16}$$

$$\tau_{i}^{A} \hat{v}_{i}^{A} \times \mathbf{v}_{i+1}^{A} = \tau_{i+3}^{A} \hat{v}_{i+3}^{A} \times \mathbf{v}_{i+2}^{A}. \tag{4.17}$$

However, because the edges bounding a face are co-planar, the orientation compatibility condition in Equation 4.16 is two-dimensional and the position compatibility condition in Equation 4.17 is one-dimensional so that the torsions also exhibit one-dimensional families of solutions. While the above constraints hold for any quadrilateral face, they are dramatically simplified for parallelograms because $\hat{v}_{i}^{A} = -\hat{v}_{i+2}^{A}$ so that the solutions take the form

$$\tau_{i}^{A} = (-1)^{i} \mathcal{F}^{A} v_{i}^{A}, \tag{4.18}$$

where, in analogy to the vertex-folding solutions in Equation 4.15, the edge lengths v_{i}^{A} are the face-bending coefficients and the scalars $\mathcal{F}^{A}$ are the face amplitudes.

These local solutions are constrained by orientation compatibility around the one-dimensional edges where a closed loop accumulates angular velocity gradients

$$\mathcal{V}^{a} \zeta_{i}^{a} + \mathcal{F}^{A} v_{j}^{A} - \mathcal{V}_{i+2}^{a'} \zeta_{i+2}^{a'} - \mathcal{F}^{A} v_{j+2}^{A'} = 0, \tag{4.19}$$

where a, a' and A, A' are respectively crease-sharing vertices and faces and the indices i, j specify this edge in the appropriate local basis. Note, for the primed vertex and face this edge index is increased by 2 because the edge is on the opposite side of the vertex of face. Thus, Equation 4.19 defines one constraint for each edge with one degree of freedom for each face and vertex, totally zero remaining degrees of freedom. Hence, by the analysis of chapter 3, there should be three isometric linear modes, quantified by the vertex and face amplitudes, that satisfy this constraint in spatially-periodic, parallelogram-based origami.

More formally, these modes are in the null space of the compatibility matrix obtained by concatenating all of the edge compatibility conditions. However, because the face-bending coefficients are simply the edge lengths, the face amplitudes can be effectively integrating out by summing the constraints on the four edges emanating from each vertex. This has two implications. The first is that the edge compatibility conditions can be rewritten as integrated vertex compatibility conditions

$$\sum \left(\frac{\zeta_{i'}^{a}}{v_{i'}^{a}} \mathcal{V}^{a} - \frac{\zeta_{i'+2}^{a'}}{v_{i'+2}^{a'}} \mathcal{V}^{a'} \right) = 0, \tag{4.20}$$

where the sum is taken over all vertices a' that join vertex a. The second is that there exists a mode comprised purely of face bending given by the trivial solutions to Equation 4.20. Thus, for any parallelogram-based origami sheet, the concatenation of this compatibility condition is a linear operator on the space of vertex amplitudes that generically has a two-dimensional null space spanned by the remaining two isometric linear modes. In subsection 4.2.2 I use the discrete symmetries of the case where the unit cell is composed of four generic parallelogram faces to characterize these two modes.

4.2.2 Discrete symmetries of the four-parallelogram origami

The formalism developed in subsection 4.2.1 applies for any spatially-periodic origami sheet composed of parallelogram faces. Extensive work in the literature has been dedicated to analyzing such sheets with four specifically chosen parallelogram faces where the isometric linear modes are obtained by triangulation [3, 2, 61, 5, 6]. These crease patterns share a common antisymmetry that permits investigation of the entire family of four-parallelogram origami simultaneously.

The degeneracy in the constraints is best captured by considering the permutation operator that exchanges non-adjacent vertices, $\mathcal{P}_d$, shown in Figure 4.5. The local edges and vertex-folding coefficients have the special transformations under this operator

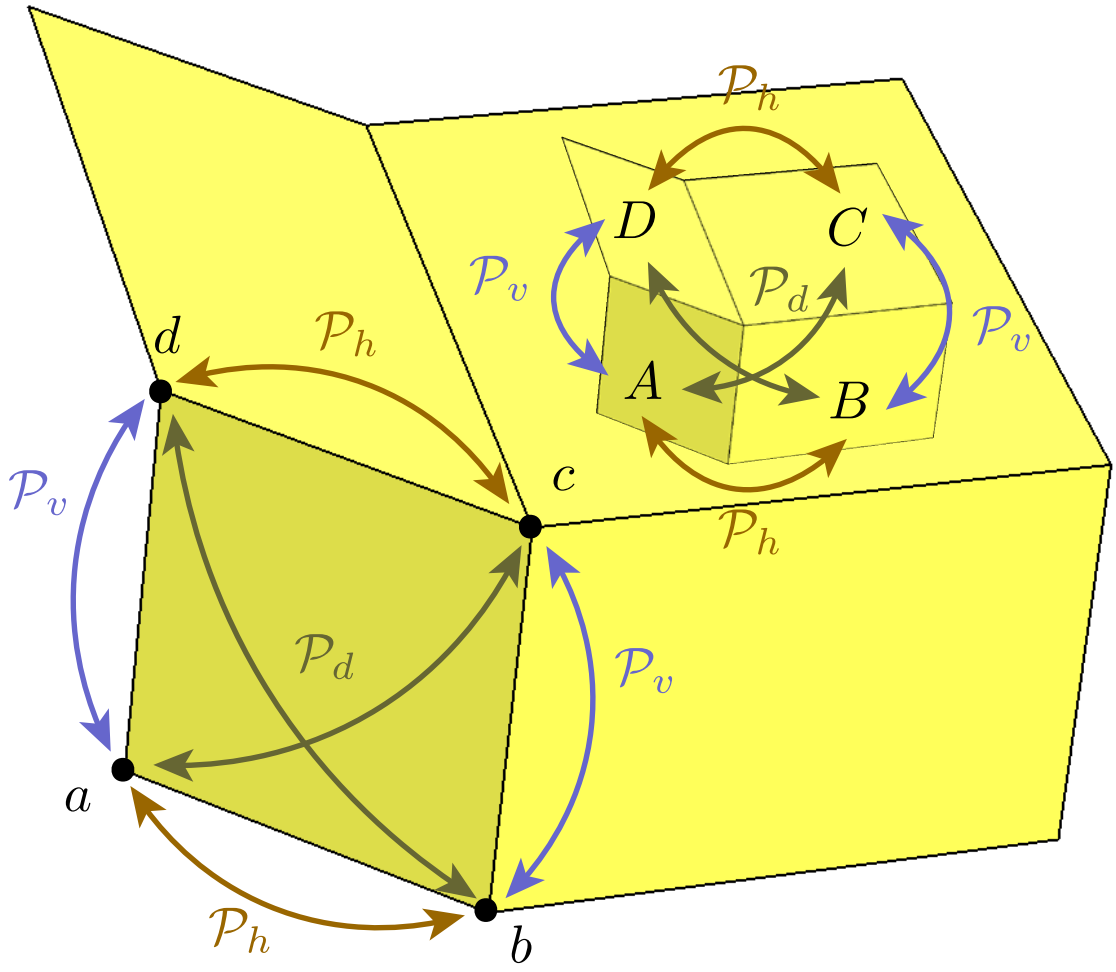

Figure 4.5: The permutation operations $\mathcal{P}_h$, $\mathcal{P}_v$, and $\mathcal{P}_d = \mathcal{P}_v\mathcal{P}_h = \mathcal{P}_h\mathcal{P}_v$ respectively swap vertices in the horizontal, vertical, and diagonal directions. The vertex folding coefficients obey the special property $\zeta_i^{\mathcal{P}_d a} = -\zeta_{i+2}^a$ under the diagonal permutation that leads to the antisymmetry and off-block diagonalization of the compatibility matrix. The faces must undergo the same permutations so that the edge compatibility condition in Equation 4.19 is invariant.

$$\mathbf{v}_i^{\mathcal{P}_d a} = -\mathbf{v}_{i+2}^a, \tag{4.21}$$

$$\zeta_i^{\mathcal{P}_d a} = -\zeta_{i+2}^a, \tag{4.22}$$

while the matrix representation of this permutation operator is real ($\mathcal{P}_d^* = \mathcal{P}_d$), symmetric ($\mathcal{P}_d^T = \mathcal{P}_d$), and orthogonal ($\mathcal{P}_d^T = \mathcal{P}_d^{-1}$) so that is unitary. Importantly, the compatibility matrix is antisymmetric under this transformation

$$\mathcal{P}_d \mathbf{C} \mathcal{P}_d = -\mathbf{C}. \tag{4.23}$$

This relationship implies that the compatibility matrix is off-block diagonalizable, a hallmark of particle-hole symmetry, into sectors that are symmetric and antisymmetric under the permutations, $\mathcal{P}_d \left|\boldsymbol{\mathcal{V}}_\pm\right\rangle = \pm \left|\boldsymbol{\mathcal{V}}_\pm\right\rangle$, as evident by the inner product

$$\langle \boldsymbol{\mathcal{V}}_\pm^{(1)} | \mathbf{C} | \boldsymbol{\mathcal{V}}_\pm^{(2)} \rangle = - \langle \boldsymbol{\mathcal{V}}_\pm^{(1)} | \mathbf{C} | \boldsymbol{\mathcal{V}}_\pm^{(2)} \rangle = 0. \tag{4.24}$$

These sectors are each two-dimensional because the diagonal permutation is composed of the horizontal and vertical permutations, $\mathcal{P}_d = \mathcal{P}_h \mathcal{P}_v = \mathcal{P}_v \mathcal{P}_h$, shown in Figure 4.5 so that symmetric (antisymmetric) modes can either be symmetric/antisymmetric under both (one) of the operations. Moreover, since these permutations commute they are simultane-

ously diagonalizable and define a convenient orthonormal basis

$$
\begin{aligned}
|SS\rangle &= \frac{1}{2}\begin{pmatrix} +1 & +1 & +1 & +1 \end{pmatrix}^T, \\
|AA\rangle &= \frac{1}{2}\begin{pmatrix} +1 & -1 & +1 & -1 \end{pmatrix}^T, \\
|SA\rangle &= \frac{1}{2}\begin{pmatrix} +1 & +1 & -1 & -1 \end{pmatrix}^T, \\
|AS\rangle &= \frac{1}{2}\begin{pmatrix} +1 & -1 & -1 & +1 \end{pmatrix}^T,
\end{aligned}
\tag{4.25}
$$

where the first (second) slot indicates the symmetry, S, or antisymmetry, A, under the $\mathcal{P}_h$ ($\mathcal{P}_v$) permutation so that linear combinations of $|SS\rangle$ and $|AA\rangle$ ($|SA\rangle$ and $|AS\rangle$) belong to the symmetric (antisymmetric) sector. This basis indeed transforms the compatibility matrix into the off-block diagonal form

$$
\mathbf{C}^{sym} = \begin{pmatrix} 0 & 0 & 0 & 0 \\ 0 & 0 & \chi_{24}^{-} & \chi_{13}^{-} \\ 0 & \chi_{24}^{-} & 0 & 0 \\ 0 & \chi_{13}^{-} & 0 & 0 \end{pmatrix}, \tag{4.26}
$$

$$
\chi_i \equiv \frac{\hat{r}_{i+1} \cdot \hat{r}_{i+2} \times \hat{r}_{i+3}}{r_i}, \tag{4.27}
$$

$$
\chi_{ij}^{\pm} \equiv \chi_i \pm \chi_j, \tag{4.28}
$$

where the χ_i are the global folding coefficients. Thus, the symmetric state, $|\boldsymbol{\mathcal{V}}\rangle = |SS\rangle$, and the antisymmetric state, $|SA\rangle - |AS\rangle$, are the two isometric linear modes that incorporate non-zero vertex folding.

The corresponding face amplitudes are obtained by substituting these solutions into the edge compatibility conditions in Equation 4.19. The differences between any pair of

vertex or face amplitudes can be written as a projection of the vertex amplitude ket onto a superposition of the basis states revealing

$$\langle \boldsymbol{\mathcal{F}} | SA \rangle = -\frac{1}{2} \chi_{13}^{+} \langle \boldsymbol{\mathcal{V}} | AS \rangle \,, \tag{4.29}$$

$$\langle \boldsymbol{\mathcal{F}} | AS \rangle = \frac{1}{2} \chi_{24}^{+} \langle \boldsymbol{\mathcal{V}} | SA \rangle \,, \tag{4.30}$$

$$\langle \boldsymbol{\mathcal{F}} | AA \rangle = -\frac{1}{2} \chi_{13}^{-} \langle \boldsymbol{\mathcal{V}} | AS \rangle \tag{4.31}$$

$$= \frac{1}{2} \chi_{24}^{-} \langle \boldsymbol{\mathcal{V}} | SA \rangle \,. \tag{4.32}$$

Note that the two symmetric vertex basis states are absent because they do not couple compatibly to face bending. Furthermore, these relationships couple the two antisymmetric vertex basis states in agreement with the coupling found in the isometric linear mode. However, they suprisingly couple both to antisymmetric *and* symmetric face amplitude states.

Using these relationships, the face amplitudes of the antisymmetric mode can be determined to write the three isometric linear modes in completeness

$$\text{Mode 1:} \quad |\boldsymbol{\mathcal{V}}_{\text{sym}}\rangle = |SS\rangle \,, \quad |\boldsymbol{\mathcal{F}}_{\text{sym}}\rangle = \mathbf{0}; \tag{4.33}$$

$$\text{Mode 2:} \quad |\boldsymbol{\mathcal{V}}_{\text{face}}\rangle = \mathbf{0}, \quad |\boldsymbol{\mathcal{F}}_{\text{face}}\rangle = |SS\rangle \,; \tag{4.34}$$

$$\text{Mode 3:} \quad \begin{aligned} |\boldsymbol{\mathcal{V}}_{\text{asym}}\rangle &= \chi_{13}^{-} |SA\rangle - \chi_{24}^{-} |AS\rangle \,, \\ |\boldsymbol{\mathcal{F}}_{\text{asym}}\rangle &= \frac{1}{2} \chi_{13}^{+} \chi_{24}^{-} |SA\rangle + \frac{1}{2} \chi_{13}^{-} \chi_{24}^{+} |AS\rangle + \frac{1}{2} \chi_{13}^{-} \chi_{24}^{-} |AA\rangle \,. \end{aligned} \tag{4.35}$$

Notably, since the angular velocity in Equation 4.11 is dimensionless, the vertex amplitudes must be dimensionless and the face amplitudes must have dimensions of inverse length. Thus, while these three modes form an orthogonal basis spanning the isometric linear modes of the four-parallelogram origami, they require additional normalization factors.

This fact is ignored in the forthcoming calculation of the lattice Poisson ratio, an observable that is independent of this normalization.

4.3 Intercellular deformations

The isometric linear modes induce strain and curvature in the periodic origami sheet. These deformations are quantified by generalizations of the fundamental forms, called *lattice fundamental forms*, that are used to define lattice Poisson ratios. Here, I show that the symmetry or antisymmetry of each mode constrains the deformations they induce revealing that the in-plane lattice Poisson ratio of the symmetric mode is equal and opposite to the out-of-plane lattice Poisson ratio of the bending mode.

4.3.1 Lattice fundamental forms and Poisson ratios

Continuous surfaces are described by the fundamental forms that geometrically couple in-plane strains with out-of-plane curvatures. Due to the lack of a smooth embedding, I introduce *lattice* fundamental forms quantified by the lattice vectors of spatially-periodic, parallelogram-based origami and use them to quantify the strains and curvatures of the isometric linear modes via changes to the periodicity.

Let the initial embedding, $\mathbf{X}$, of the origami be the average vertex position in each cell and take the cell index as the surface coordinates

$$\mathbf{X}(\mathbf{n}) = \sum_{\mu} n^{\mu} \boldsymbol{\ell}_{\mu}, \tag{4.36}$$

with the assumption that the average vertex position in cell $(0, 0)$ is the origin. The corresponding tangent vectors of this embedding are the lattice vectors, $\partial_{\mu}\mathbf{X} = \boldsymbol{\ell}_{\mu}$, thereby defining the first lattice fundamental form

$$I_{\mu\nu} \equiv (\partial_{\mu}\mathbf{X}) \cdot (\partial_{\nu}\mathbf{X}) = \boldsymbol{\ell}_{\mu} \cdot \boldsymbol{\ell}_{\nu}. \tag{4.37}$$

Similarly, the corresponding curvatures are inversely proportional to the changes in the lattice vectors, $\partial_\mu \partial_\nu \mathbf{X} = \partial_\mu \boldsymbol{\ell}_\nu$, thereby defining the second lattice fundamental form

$$II_{\mu\nu} \equiv \hat{n} \cdot \partial_\mu \partial_\nu \mathbf{X} = \hat{n} \cdot \big(\boldsymbol{\ell}_\nu(n^\mu = 1) - \boldsymbol{\ell}_\nu(n^\mu = 0) \big) \tag{4.38}$$

which vanishes for the spatially periodic configurations considered here.

The isometric linear modes change the lattice fundamental forms due to changes in the lattice vectors

$$\boldsymbol{\Delta}_\mu^{a,A} \equiv \mathbf{u}^{a,A}(n^\mu = 1) - \mathbf{u}^{a,A}(n^\mu = 0), \tag{4.39}$$

where the superscripts emphasize the fact that these are locally defined as they are measured from a particular corner. Moreover, the isometric linear modes can induce intracell rotations captured by the lattice angular velocities

$$\boldsymbol{\Omega}_\mu \equiv \boldsymbol{\omega}^{a,A}(n^\mu = 1) - \boldsymbol{\omega}^{a,A}(n^\mu = 0). \tag{4.40}$$

Importantly, the local dependence of these lattice vector changes couples to the lattice angular velocities due to compatibility along the path shown in Figure 4.6(a)

$$\boldsymbol{\Delta}_\mu^{a',A'} - \boldsymbol{\Delta}_\mu^{a,A} = \boldsymbol{\Omega}_\mu \times \mathbf{r}_{aa'} + \boldsymbol{\omega}_{a,A}^{a',A'} \times \boldsymbol{\ell}_\mu, \tag{4.41}$$

where $\mathbf{r}_{aa'}$ points from vertex a to vertex a' and $\boldsymbol{\omega}_{a,A}^{a',A'}$ is the angular velocity gradient between corners (a, A) and (a', A'). This yields a useful connection between the in-plane strains and out-of-plane curvatures in the origami sheet, similar to that for an elastic slab as demonstrated in Figure 4.6(b).

Since our initial embedding is defined by the average vertex position in each cell, changes in the first lattice fundamental form do not privilege any particular vertex. Thus,

the changes in the first fundamental form are written

$$\delta I_{\mu\nu} = \bar{\boldsymbol{\Delta}}_\mu \cdot \boldsymbol{\ell}_\nu + \boldsymbol{\ell}_\mu \cdot \bar{\boldsymbol{\Delta}}_\nu, \tag{4.42}$$

where $\bar{\boldsymbol{\Delta}}_\mu$ is the change in the lattice vector averaged over all corners. However, the distinction between the change in the lattice vector, $\boldsymbol{\Delta}_\mu$, at any corners (a, A) and (a, A') vanishes when projected onto the same lattice vector, $\boldsymbol{\ell}_\mu$, and cancels by symmetrizing over opposite lattice vectors. Thus, the projections

$$\bar{\boldsymbol{\Delta}}_\mu \cdot \boldsymbol{\ell}_\nu + \bar{\boldsymbol{\Delta}}_\nu \cdot \boldsymbol{\ell}_\mu = \sum_a \left(\boldsymbol{\Delta}_\mu^a \cdot \boldsymbol{\ell}_\nu + \boldsymbol{\Delta}_\nu^a \cdot \boldsymbol{\ell}_\mu \right), \tag{4.43}$$

only need to be averaged over the vertices.

Expansion of the second lattice fundamental form in Equation 4.38 yields

$$\delta II_{\mu\nu} = \hat{n} \cdot (\boldsymbol{\Omega}_\mu \times \boldsymbol{\ell}_\nu), \tag{4.44}$$

which does not exhibit any immediate connections to changes in the first lattice fundamental form, as might be expected from the Gauss-Codazzi equations for continuous sheets [20]. However, applying Equation 4.41 and noting that position compatibility ensures $\boldsymbol{\Omega}_\mu \times \boldsymbol{\ell}_\nu$ always lies in the normal direction and is symmetric under swapping μ and ν to rewrite the second lattice fundamental form

$$\delta II_{\mu\nu} = -\frac{\left(\boldsymbol{\Delta}_\mu^{a'} - \boldsymbol{\Delta}_\mu^a \right) \cdot \boldsymbol{\ell}_\nu + \left(\boldsymbol{\Delta}_\nu^{a'} - \boldsymbol{\Delta}_\nu^a \right) \cdot \boldsymbol{\ell}_\mu}{2\mathbf{r}_{aa'} \cdot \hat{n}}. \tag{4.45}$$

The diagonal components of these changes to the lattice fundamental forms characterize the stretching and curvature of the lattice in transverse cell directions. Thus, these quantities naturally define the lattice Poisson ratios

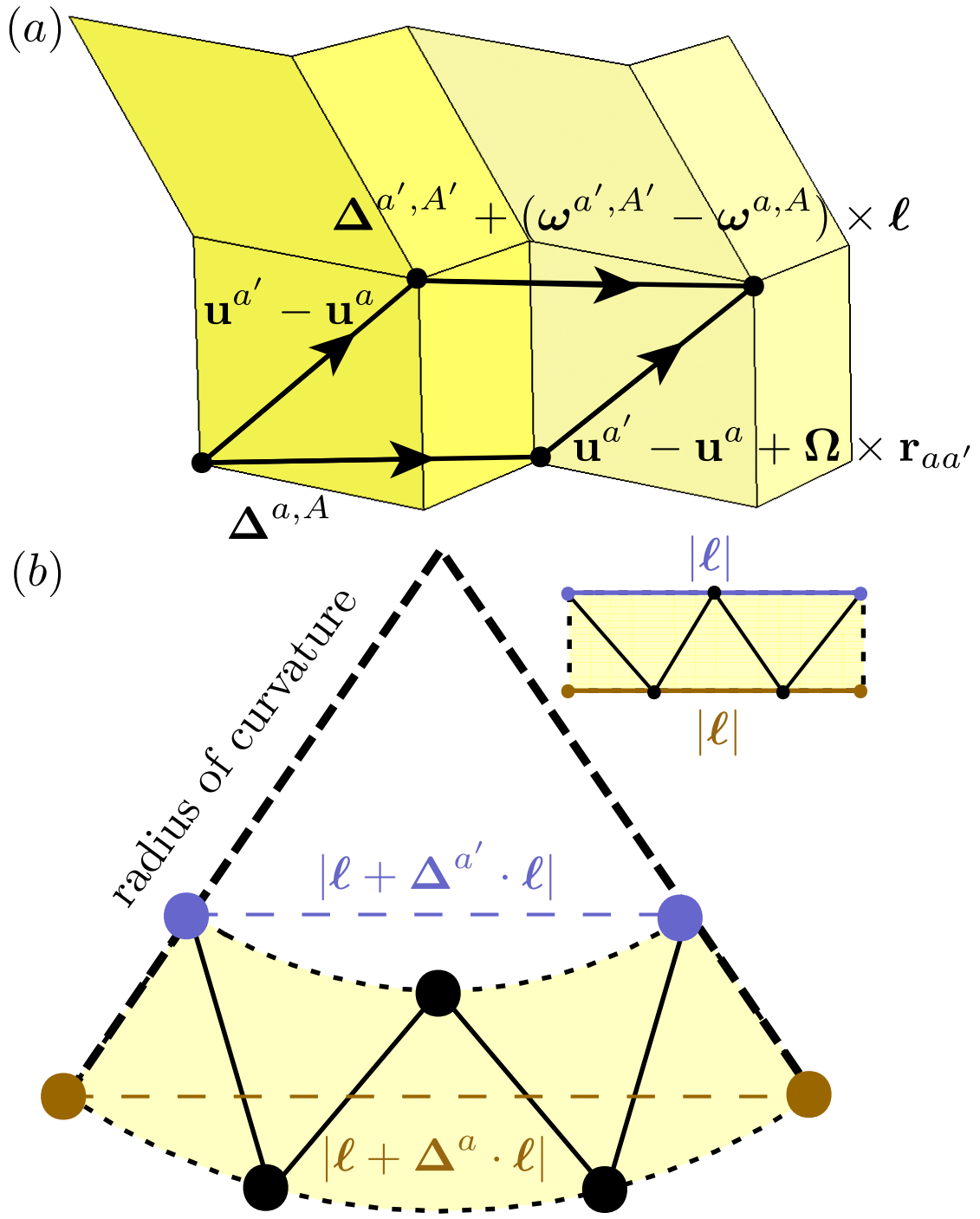

Figure 4.6: (a) The difference in the locally measured changes to the lattice vector is related, by position compatibility, to the lattice angular velocity according to Equation 4.41. This changes in the second lattice fundamental form to be written as functions of the changes in the lattice vectors and hence, couples changes in the two lattice fundamental forms to one another. (b) The local dependence of the changes in the lattice vectors parallels to the bending of an elastic slab. As a slab is bend upwards out of plane, the top of the slab compresses while the bottom of the slab stretches so that there is no strain in the neutral mid-plane of the slab. For the origami, this neutral mid-plane is determined by the average vertex position.

$$\nu_{\text{in}} \equiv -\frac{|\boldsymbol{\ell}_2|^2}{|\boldsymbol{\ell}_1|^2}\frac{\bar{\boldsymbol{\Delta}}_{11}\cdot\boldsymbol{\ell}_1}{\bar{\boldsymbol{\Delta}}_{22}\cdot\boldsymbol{\ell}_2}, \tag{4.46}$$

$$\nu_{\text{out}} \equiv -\frac{|\boldsymbol{\ell}_2|^2}{|\boldsymbol{\ell}_1|^2}\frac{(\boldsymbol{\Delta}^a_{11}-\boldsymbol{\Delta}^{a'}_{11})\cdot\boldsymbol{\ell}_1}{(\boldsymbol{\Delta}^a_{22}-\boldsymbol{\Delta}^{a'}_{22})\cdot\boldsymbol{\ell}_2}. \tag{4.47}$$

The antisymmetry of the four-parallelogram origami leads to an intimate connection between these two quantities for the symmetric and antisymmetric modes discussed in subsection 4.3.2.

4.3.2 Equal and opposite lattice Poisson ratios in the four-parallelogram

The changes in the lattice fundamental forms and the lattice Poisson ratios are defined for generic parallelogram-based origami. The same antisymmetry that off-block diagonalizes the compatibility matrix in the four-parallelogram origami governs these quantities so that they take simple forms for each of the isometric linear modes.

Changes in both the first and second lattice fundamental forms are dependent on the projections of changes into the lattice vectors onto the initial lattice vectors. The simplifying feature of the four-parallelogram origami is that these locally-defined quantities only vary between vertices by factors of the vertex amplitudes which can be seen by computing them explicitly in an arbitrary local basis.

Without loss of generality, let this local basis be defined at vertex a. The measured lattice vector changes are

$$\boldsymbol{\Delta}^a_1 = \left(\tau_1^A\hat{v}_1^a - \phi_2^{\mathcal{P}_h a}\hat{v}_2^{\mathcal{P}_h a}\right)\times\mathbf{v}_1^{\mathcal{P}_h a}, \tag{4.48}$$

$$\boldsymbol{\Delta}^a_2 = \left(\tau_4^A\hat{v}_2^a + \phi_1^{\mathcal{P}_v a}\hat{v}_1^{\mathcal{P}_v a}\right)\times\mathbf{v}_2^{\mathcal{P}_v a}. \tag{4.49}$$

In this local basis, the lattice vectors can be written $\boldsymbol{\ell}_1 = \mathbf{v}_1^a - \mathbf{v}_3^a, \boldsymbol{\ell}_2 = \mathbf{v}_2^a - \mathbf{v}_4^a$, so that

the diagonal projections take the form

$$\boldsymbol{\Delta}_1^a \cdot \boldsymbol{\ell}_1 = -\mathcal{V}^{\mathcal{P}_h a} v_1^{\mathcal{P}_h a} v_3^{\mathcal{P}_h a} \zeta_2^{\mathcal{P}_h a} \zeta_4^{\mathcal{P}_h a}, \tag{4.50}$$

$$\boldsymbol{\Delta}_2^a \cdot \boldsymbol{\ell}_2 = \mathcal{V}^{\mathcal{P}_v a} v_2^{\mathcal{P}_v a} v_4^{\mathcal{P}_v a} \zeta_1^{\mathcal{P}_v a} \zeta_3^{\mathcal{P}_v a}, \tag{4.51}$$

where I have used the symmetries of the horizontal and vertical permutations

$$\mathbf{v}_i^{\mathcal{P}_h a} = \begin{cases} \mathbf{v}_i^a, & \text{for } i \text{ even} \\ -\mathbf{v}_{i+2}^a, & \text{for } i \text{ odd} \end{cases}, \qquad \mathbf{v}_i^{\mathcal{P}_v a} = \begin{cases} \mathbf{v}_i^a, & \text{for } i \text{ odd} \\ -\mathbf{v}_{i+2}^a, & \text{for } i \text{ even} \end{cases}, \tag{4.52}$$

$$\zeta_i^{\mathcal{P}_h a} = \begin{cases} -\zeta_i^a, & \text{for } i \text{ even} \\ \zeta_{i+2}^a, & \text{for } i \text{ odd} \end{cases}, \qquad \zeta_i^{\mathcal{P}_v a} = \begin{cases} -\zeta_i^a, & \text{for } i \text{ odd} \\ \zeta_{i+2}^a, & \text{for } i \text{ even} \end{cases}. \tag{4.53}$$

These pairings of edges and vertex folding coefficients are invariant under all permutations so that the projections of the lattice vectors change only by a factor of the vertex amplitude when measured from a different vertex. Hence, the projections can be rewritten in terms of the global folding coefficients

$$\boldsymbol{\Delta}_1^a \cdot \boldsymbol{\ell}_1 = R\chi_2\chi_4 \left\langle a | \mathcal{P}_h | \boldsymbol{\mathcal{V}} \right\rangle, \tag{4.54}$$

$$\boldsymbol{\Delta}_2^a \cdot \boldsymbol{\ell}_2 = -R\chi_1\chi_3 \left\langle a | \mathcal{P}_v | \boldsymbol{\mathcal{V}} \right\rangle. \tag{4.55}$$

Thus, the decomposition of the modes into symmetric and antisymmetric sectors naturally divides the modes into ones that exclusively generate strains and ones that exclusively generate curvature. First, consider changes to the diagonal components of the first lattice fundamental form, Equation 4.42, obtained by averaging over all vertices a in Eqs.

(Equation 4.54, Equation 4.55). The effect is to replace the sum over the particular vector, $\sum \langle a'|$, with the symmetric state , $\langle SS|$, so that only the symmetric mode can stretch or compress the lattice vectors. Next, consider changes to the diagonal components of the second lattice fundamental form, Equation 4.45, obtained by taking the difference of Eqs. (Equation 4.54, Equation 4.55) between any pair of vertices. Without loss of generality, we choose the non-adjacent pair of vertices, $\langle a| - \langle c|$, that are equal to the antisymmetric combination, $\langle SA| + \langle AS|$, indicating that only the antisymmetric mode can curve the lattice vectors.

Finally, consider the corresponding in-plane and out-of-plane lattice Poisson ratios computed via Eqs. (Equation 4.46, Equation 4.47) respectively. While changes in the first and second lattice fundamental forms are themselves distinct because of the different geometry associated with stretching and curving, the distinct prefactors cancel when taking their ratio. The only distinction is that where the numerator contains a factor of $\mathcal{P}_h \left|\boldsymbol{\mathcal{V}}\right\rangle$, the denominator contains a factor of $\mathcal{P}_v \left|\boldsymbol{\mathcal{V}}\right\rangle = \mathcal{P}_d\mathcal{P}_h \left|\boldsymbol{\mathcal{V}}\right\rangle$ which generates a relative factor of -1 for the antisymmetric mode. Consequently, the in-plane and out-of-plane Poisson ratios of the three isometric linear modes of a given four-parallelogram configuration contain only a single value, whose sign is flipped for the antisymmetric modes relative to that of the symmetric modes. In fact, because so many of the aforementioned components of the fundamental forms are conserved under the modes most of the Poisson ratios are ill-defined, leaving only the equal and opposite in-plane Poisson ratio of the symmetric mode and the out-of-plane Poisson ratio of the antisymmetric mode:

$$\nu_{\text{out}}^{\text{asym}} = -\nu_{\text{in}}^{\text{sym}} = -\frac{|\boldsymbol{\ell}_2|^2}{|\boldsymbol{\ell}_1|^2}\frac{\chi_2\chi_4}{\chi_1\chi_3}. \tag{4.56}$$

This result, which has been previously obtained via alternate means for the Miura-ori [61, 2], the eggbox [5], and the Morph [6] follows purely from the antisymmetry of the unit cell

under the diagonal vertex exchange shown in Fig. Figure 4.5.

This antisymmetry justifies the fact that the four-parallelogram origami has two lattice Poisson ratios with opposite signs in contrasts to the case of the elastic slab, as sketched in Figure 4.6, where the in-plane and out-of-plane Poisson ratios are equal. In particular, the slab exhibits a single mode that couples in-plane strains with out-of-plane curvatures whereas the stretching and bending of the origami sheet arise from two linearly independent modes due to the existence of symmetry and antisymmetry sectors.

4.4 Discussion

I have explored the family of periodic origami composed of four parallelogram faces per cell. I showed that such patterns generically have a one-dimensional surface of spatially-periodic degenerate ground states. I also derived compatibility conditions on the linear isometries and used a discrete symmetry of the crease pattern to decompose the resulting compatibility matrix into symmetric and antisymmetric sectors. Finally, I showed that modes in the symmetric (antisymmetric) sector exhibit purely in-plane strain (out-of-plane curvature) and the two modes have equal and opposite lattice Poisson ratios.

The formalism developed in this chapter captures all of the linear isometries of quadrilateral-based crease patterns while making discrete symmetries more apparent than the corresponding triangulations. Thus, in addition to the interesting result for the four-parallelogram family, there are immediate extensions of interest. First, the nonuniform modes of the four-parallelogram should be investigated to search for any role of the permutation symmetry on the band structure, particularly the existence of any high-symmetry points that may indicate special modes which correspond to symmetry breaking. Second, the formalism can be directly applied to crease patterns composed of more than four parallelogram faces, such as the block fold, which may exhibit more involved symmetries yet fall in the same class due to the action of these symmetries on the compatibility matrix. Third, I have solved the face compatibility condition in Equation 4.16 and Equation 4.17 exclusively for parallelo-

gram faces; determining the solution for more generic quadrilaterals permits the symmetry analysis of such patterns. Notably, other quadrilateral-based crease patterns are generically screw-periodic and hence, they likely belong to a different classification of compatibility matrices. Lastly, the face-bending and antisymmetric modes induce non-cylindrical curvatures so that they do not uniformly extend to second order. However, allowing these modes to spatially vary may reveal soft modes observable in physical origami sheets.

CHAPTER 5
DISCUSSION

I have presented results for two broad classes of periodic origami. First, I have discussed Maxwell origami - triangulations with equal numbers of constraints and degrees of freedom - to show that a hidden symmetry generates a two-dimensional space of degenerate ground states and that its linear compatibility matrix belongs to a special topological class. Second, I have discussed four-parallelogram origami - sheets composed of unit cells with four parallelogram faces - to show that a discrete symmetry constrains the modes and their mechanical response so that such sheets always possess one negative Poisson ratio mode. I have emphasized the role of determining these properties by the mathematical properties of the linear compatibility matrix, similar to the classification of Hamiltonians for topological insulators and super conductors [15, 16, 17, 18, 19]. Here, I discuss some immediate extensions to these efforts.

The topological classification of Maxwell origami via the realness property of its linear compatibility matrix means that its winding number vanishes; however, this class of matrices still admit non-trivial topological invariants [88]. First, the zeroeth homotopy group possesses a Z_2 invariant that can be computed by the sign of the determinant of the compatibility matrix. In principle, a non-uniform Maxwell origami crease pattern could exhibit topologically protected modes at a boundary between $+1$ and -1 phases, however I have been unable to tune a crease pattern to undergo this transition in real space. Second, the first homotopy group (computed by the winding number for complex matrices) also possess a Z_2 invariant and could similarly be used to determine the existence of topologically protected modes. However, here I have been unable to compute this topological invariant for generics-sized compatibility matrices. The most promising extension might be to use the fact that the emergence of a third continuous symmetry in the spatially periodic

state indicates the elimination of a band gap. Hence, a sheet that spatially varies from an upwards folded cylinder to a downwards folded cylinder could exhibit topologically protected modes at the interface between these two regions as governed by the Z_2 invariant corresponding to the sign of the curvature.

The antisymmetry of the linear compatibility matrix for the four-parallelogram origami implied the existence of distinct sectors of uniform modes that consequently had distinct mechanical responses. This analysis could be extended to nonuniform modes where the discrete symmetry may yield high symmetry points in the Brillouin zone that exhibit interesting mechanical response due to symmetry breaking. Moreover, such nonuniform modes could be used to accommodate the curvature induced by the asymmetric mode so that the deformations extend to second order. Lastly, the formalism could be applied to more general patterns including those with more than four parallelogram faces, such as the block fold, as well as those with non-parallelogram faces, provided the face compatibility conditions are resolved. Since quadrilateral-based origami crease patterns rely on discrete symmetries to rigidly fold, this analysis could reveal common features between seemingly distinct crease patterns.

The reduction from a continuum model of elastic sheets to geometric compatibility conditions is paramount to the content of this thesis and the analytical results on origami crease patterns herein. While this simplification indeed matches with finite element simulations for linear deformations [13, 56], physical crease patterns exhibit additional mechanical properties that make experimental validation difficult. First, physical sheets have finite elastic moduli that dictate the energy cost for crease folding, face bending, and face stretching. Importantly, this crease folding modulus depends not only on the material parameters but also on the characteristic dimensions of the creases and faces, thereby impacting the scalability for rigidly foldable patterns [103]. Moreover, these elastic moduli are the coefficients for energy functionals that depend on reference configuration of a crease pattern [104, 105] so that for certain geometries and material parameters there exist bistable configura-

tions [104, 96]. Second, individual creases obey logarithmic relaxation times when they are strained [106] and moreover, relax to different reference angle [107]. Lastly, the energy cost of folding creases implies that locally actuated folding motions decay across the sheet, revealing strain reversal, where cells contract or expand oppositely to the actuated cell, due to finite bending moduli [108]. Thus, corrections must be made to the geometric description of origami in order to quantitatively, and not just qualitatively, predict the nonlinear, dynamical mechanical response with localized actuation and real materials while maintaining analytical tractability.

REFERENCES

[1] R. J. Lang, "The science of origami," *Physics world*, vol. 20, no. 2, p. 30, 2007.

[2] Z. Y. Wei, Z. V. Guo, L. Dudte, H. Y. Liang, and L. Mahadevan, "Geometric mechanics of periodic pleated origami," *Physical review letters*, vol. 110, no. 21, p. 215 501, 2013.

[3] M. Schenk and S. D. Guest, "Origami folding: A structural engineering approach," *Origami*, vol. 5, pp. 291–304, 2011.

[4] C. Lv, D. Krishnaraju, G. Konjevod, H. Yu, and H. Jiang, "Origami based mechanical metamaterials," *Scientific reports*, vol. 4, no. 1, pp. 1–6, 2014.

[5] H. Nassar, A. Lebée, and L. Monasse, "Curvature, metric and parametrization of origami tessellations: Theory and application to the eggbox pattern," *Proceedings of the Royal Society A: Mathematical, Physical and Engineering Sciences*, vol. 473, no. 2197, p. 20 160 705, 2017.

[6] P. P. Pratapa, K. Liu, and G. H. Paulino, "Geometric mechanics of origami patterns exhibiting poisson's ratio switch by breaking mountain and valley assignment," *Physical review letters*, vol. 122, no. 15, p. 155 501, 2019.

[7] E. T. Filipov, T. Tachi, and G. H. Paulino, "Origami tubes assembled into stiff, yet reconfigurable structures and metamaterials," *Proceedings of the National Academy of Sciences*, vol. 112, no. 40, pp. 12 321–12 326, 2015.

[8] J. Ma and Z. You, "The origami crash box," *Origami*, vol. 5, pp. 277–290, 2011.

[9] X. Zhou, S. Zang, and Z. You, "Origami mechanical metamaterials based on the miura-derivative fold patterns," *Proceedings of the Royal Society A: Mathematical, Physical and Engineering Sciences*, vol. 472, no. 2191, p. 20 160 361, 2016.

[10] H. Yasuda and J. Yang, "Reentrant origami-based metamaterials with negative poisson's ratio and bistability," *Physical review letters*, vol. 114, no. 18, p. 185 502, 2015.

[11] S. Kamrava, D. Mousanezhad, H. Ebrahimi, R. Ghosh, and A. Vaziri, "Origami-based cellular metamaterial with auxetic, bistable, and self-locking properties," *Scientific reports*, vol. 7, no. 1, pp. 1–9, 2017.

[12] C. D. Santangelo, "Extreme mechanics: Self-folding origami," *Annual Review of Condensed Matter Physics*, vol. 8, pp. 165–183, 2017.

[13] E. Filipov, K. Liu, T. Tachi, M. Schenk, and G. H. Paulino, "Bar and hinge models for scalable analysis of origami," *International Journal of Solids and Structures*, vol. 124, pp. 26–45, 2017.

[14] H. A. Akitaya, E. D. Demaine, T. Horiyama, T. C. Hull, J. S. Ku, and T. Tachi, "Rigid foldability is np-hard," *Journal of computational geometry*, vol. 11, no. 1, 2020.

[15] A. Altland and M. R. Zirnbauer, "Nonstandard symmetry classes in mesoscopic normal-superconducting hybrid structures," *Physical Review B*, vol. 55, no. 2, p. 1142, 1997.

[16] A. P. Schnyder, S. Ryu, A. Furusaki, and A. W. Ludwig, "Classification of topological insulators and superconductors in three spatial dimensions," *Physical Review B*, vol. 78, no. 19, p. 195 125, 2008.

[17] A. Kitaev, "Periodic table for topological insulators and superconductors," in *AIP conference proceedings*, American Institute of Physics, vol. 1134, 2009, pp. 22–30.

[18] S. Ryu, A. P. Schnyder, A. Furusaki, and A. W. Ludwig, "Topological insulators and superconductors: Tenfold way and dimensional hierarchy," *New Journal of Physics*, vol. 12, no. 6, p. 065 010, 2010.

[19] C.-K. Chiu, J. C. Teo, A. P. Schnyder, and S. Ryu, "Classification of topological quantum matter with symmetries," *Reviews of Modern Physics*, vol. 88, no. 3, p. 035 005, 2016.

[20] D. Lovelock and H. Rund, *Tensors, differential forms, and variational principles*. Courier Corporation, 1989.

[21] Y. Klein, E. Efrati, and E. Sharon, "Shaping of elastic sheets by prescription of non-euclidean metrics," *Science*, vol. 315, no. 5815, pp. 1116–1120, 2007.

[22] T. A. Witten, "Stress focusing in elastic sheets," *Reviews of Modern Physics*, vol. 79, no. 2, p. 643, 2007.

[23] L. Mahadevan and S. Rica, "Self-organized origami," *Science*, vol. 307, no. 5716, pp. 1740–1740, 2005.

[24] X. Chen and J. W. Hutchinson, "A family of herringbone patterns in thin films," *Scripta materialia*, vol. 50, no. 6, pp. 797–801, 2004.

[25] ——, "Herringbone buckling patterns of compressed thin films on compliant substrates," *J. Appl. Mech.*, vol. 71, no. 5, pp. 597–603, 2004.

[26] B. Audoly and A. Boudaoud, "Buckling of a stiff film bound to a compliant substrate—part i:: Formulation, linear stability of cylindrical patterns, secondary bifurcations," *Journal of the Mechanics and Physics of Solids*, vol. 56, no. 7, pp. 2401–2421, 2008.

[27] ——, "Buckling of a stiff film bound to a compliant substrate—part ii:: A global scenario for the formation of herringbone pattern," *Journal of the Mechanics and Physics of Solids*, vol. 56, no. 7, pp. 2422–2443, 2008.

[28] ——, "Buckling of a stiff film bound to a compliant substrate—part iii:: Herringbone solutions at large buckling parameter," *Journal of the Mechanics and Physics of Solids*, vol. 56, no. 7, pp. 2444–2458, 2008.

[29] R. V. Kohn and H.-M. Nguyen, "Analysis of a compressed thin film bonded to a compliant substrate: The energy scaling law," *Journal of nonlinear science*, vol. 23, no. 3, pp. 343–362, 2013.

[30] K. Miura, "Method of packaging and deployment of large membranes in space," *The Institute of Space and Astronautical Science report*, no. 618, pp. 1–9, 1985.

[31] ——, "The science of miura-ori: A review," *Origami*, vol. 4, pp. 87–99, 2009.

[32] L. H. Dudte, E. Vouga, T. Tachi, and L. Mahadevan, "Programming curvature using origami tessellations," *Nature materials*, vol. 15, no. 5, pp. 583–588, 2016.

[33] E. Hawkes, B. An, N. M. Benbernou, H. Tanaka, S. Kim, E. D. Demaine, D. Rus, and R. J. Wood, "Programmable matter by folding," *Proceedings of the National Academy of Sciences*, vol. 107, no. 28, pp. 12 441–12 445, 2010.

[34] S. M. Felton, M. T. Tolley, B. Shin, C. D. Onal, E. D. Demaine, D. Rus, and R. J. Wood, "Self-folding with shape memory composites," *Soft Matter*, vol. 9, no. 32, pp. 7688–7694, 2013.

[35] S. Felton, M. Tolley, E. Demaine, D. Rus, and R. Wood, "A method for building self-folding machines," *Science*, vol. 345, no. 6197, pp. 644–646, 2014.

[36] M. T. Tolley, S. M. Felton, S. Miyashita, D. Aukes, D. Rus, and R. J. Wood, "Self-folding origami: Shape memory composites activated by uniform heating," *Smart Materials and Structures*, vol. 23, no. 9, p. 094 006, 2014.

[37] N. Bassik, G. M. Stern, and D. H. Gracias, "Microassembly based on hands free origami with bidirectional curvature," *Applied physics letters*, vol. 95, no. 9, p. 091 901, 2009.

[38] J. Kim, J. A. Hanna, M. Byun, C. D. Santangelo, and R. C. Hayward, "Designing responsive buckled surfaces by halftone gel lithography," *Science*, vol. 335, no. 6073, pp. 1201–1205, 2012.

[39] Y. Liu, J. Genzer, and M. D. Dickey, ""2d or not 2d": Shape-programming polymer sheets," *Progress in Polymer Science*, vol. 52, pp. 79–106, 2016.

[40] Y. Liu, J. K. Boyles, J. Genzer, and M. D. Dickey, "Self-folding of polymer sheets using local light absorption," *Soft matter*, vol. 8, no. 6, pp. 1764–1769, 2012.

[41] J.-H. Na, A. A. Evans, J. Bae, M. C. Chiappelli, C. D. Santangelo, R. J. Lang, T. C. Hull, and R. C. Hayward, "Programming reversibly self-folding origami with micropatterned photo-crosslinkable polymer trilayers," *Advanced Materials*, vol. 27, no. 1, pp. 79–85, 2015.

[42] J. Rogers, Y. Huang, O. G. Schmidt, and D. H. Gracias, "Origami mems and nems," *Mrs Bulletin*, vol. 41, no. 2, pp. 123–129, 2016.

[43] J. Ryu, M. D'Amato, X. Cui, K. N. Long, H. Jerry Qi, and M. L. Dunn, "Photo-origami—bending and folding polymers with light," *Applied Physics Letters*, vol. 100, no. 16, p. 161 908, 2012.

[44] Z. Lin, L. S. Novelino, H. Wei, N. A. Alderete, G. H. Paulino, H. D. Espinosa, and S. Krishnaswamy, "Folding at the microscale: Enabling multifunctional 3d origami-architected metamaterials," *Small*, vol. 16, no. 35, p. 2 002 229, 2020.

[45] Q. Ge, C. K. Dunn, H. J. Qi, and M. L. Dunn, "Active origami by 4d printing," *Smart materials and structures*, vol. 23, no. 9, p. 094 007, 2014.

[46] J. L. Silverberg, J.-H. Na, A. A. Evans, B. Liu, T. C. Hull, C. D. Santangelo, R. J. Lang, R. C. Hayward, and I. Cohen, "Origami structures with a critical transition to bistability arising from hidden degrees of freedom," *Nature materials*, vol. 14, no. 4, pp. 389–393, 2015.

[47] M. Z. Miskin, K. J. Dorsey, B. Bircan, Y. Han, D. A. Muller, P. L. McEuen, and I. Cohen, "Graphene-based bimorphs for micron-sized, autonomous origami machines," *Proceedings of the National Academy of Sciences*, vol. 115, no. 3, pp. 466–470, 2018.

[48] H. Chen, X.-L. Zhang, Y.-Y. Zhang, D. Wang, D.-L. Bao, Y. Que, W. Xiao, S. Du, M. Ouyang, S. T. Pantelides, *et al.*, "Atomically precise, custom-design origami graphene nanostructures," *Science*, vol. 365, no. 6457, pp. 1036–1040, 2019.

[49] K. J. Si, D. Sikdar, Y. Chen, F. Eftekhari, Z. Xu, Y. Tang, W. Xiong, P. Guo, S. Zhang, Y. Lu, *et al.*, "Giant plasmene nanosheets, nanoribbons, and origami," *ACS nano*, vol. 8, no. 11, pp. 11 086–11 093, 2014.

[50] L. D. Landau, E. M. Lifshitz, *et al.*, *Theory of elasticity*, 3. Pergamon Press, Oxford New York, 1986, vol. 7.

[51] B. Thiria and M. Adda-Bedia, "Relaxation mechanisms in the unfolding of thin sheets," *Physical review letters*, vol. 107, no. 2, p. 025 506, 2011.

[52] S. W. Grey, F. Scarpa, and M. Schenk, "Strain reversal in actuated origami structures," *Physical review letters*, vol. 123, no. 2, p. 025 501, 2019.

[53] F. Lechenault, B. Thiria, and M. Adda-Bedia, "Mechanical response of a creased sheet," *Physical review letters*, vol. 112, no. 24, p. 244 301, 2014.

[54] D. A. Huffman, "Curvature and creases: A primer on paper," *IEEE Computer Architecture Letters*, vol. 25, no. 10, pp. 1010–1019, 1976.

[55] T. C. Hull *et al.*, "Modelling the folding of paper into three dimensions using affine transformations," *Linear Algebra and its applications*, vol. 348, no. 1-3, pp. 273–282, 2002.

[56] K. Liu and G. Paulino, "Nonlinear mechanics of non-rigid origami: An efficient computational approach," *Proceedings of the Royal Society A: Mathematical, Physical and Engineering Sciences*, vol. 473, no. 2206, p. 20 170 348, 2017.

[57] A. A. Evans, J. L. Silverberg, and C. D. Santangelo, "Lattice mechanics of origami tessellations," *Physical Review E*, vol. 92, no. 1, p. 013 205, 2015.

[58] M. B. Pinson, M. Stern, A. C. Ferrero, T. A. Witten, E. Chen, and A. Murugan, "Self-folding origami at any energy scale," *Nature communications*, vol. 8, p. 15 477, 2017.

[59] K. Liu, L. S. Novelino, P. Gardoni, and G. H. Paulino, "Big influence of small random imperfections in origami-based metamaterials," *Proceedings of the Royal Society A*, vol. 476, no. 2241, p. 20 200 236, 2020.

[60] S. Waitukaitis, R. Menaut, B. G.-g. Chen, and M. Van Hecke, "Origami multistability: From single vertices to metasheets," *Physical review letters*, vol. 114, no. 5, p. 055 503, 2015.

[61] M. Schenk and S. D. Guest, "Geometry of miura-folded metamaterials," *Proceedings of the National Academy of Sciences*, vol. 110, no. 9, pp. 3276–3281, 2013.

[62] A. J. Liu and S. R. Nagel, "Jamming is not just cool any more," *Nature*, vol. 396, no. 6706, pp. 21–22, 1998.

[63] ——, "The jamming transition and the marginally jammed solid," *Annu. Rev. Condens. Matter Phys.*, vol. 1, no. 1, pp. 347–369, 2010.

[64] S. Feng and P. N. Sen, "Percolation on elastic networks: New exponent and threshold," *Physical review letters*, vol. 52, no. 3, p. 216, 1984.

[65] D. J. Jacobs and M. F. Thorpe, "Generic rigidity percolation: The pebble game," *Physical review letters*, vol. 75, no. 22, p. 4051, 1995.

[66] D. Jacobs and M. Thorpe, "Generic rigidity percolation in two dimensions," *Physical Review E*, vol. 53, no. 4, p. 3682, 1996.

[67] J. C. Maxwell, "L. on the calculation of the equilibrium and stiffness of frames," *The London, Edinburgh, and Dublin Philosophical Magazine and Journal of Science*, vol. 27, no. 182, pp. 294–299, 1864.

[68] R. Connelly and W. Whiteley, "Second-order rigidity and prestress stability for tensegrity frameworks," *SIAM Journal on Discrete Mathematics*, vol. 9, no. 3, pp. 453–491, 1996.

[69] C. R. Barker, "A complete classification of planar four-bar linkages," *Mechanism and Machine Theory*, vol. 20, no. 6, pp. 535–554, 1985.

[70] B. G.-g. Chen, N. Upadhyaya, and V. Vitelli, "Nonlinear conduction via solitons in a topological mechanical insulator," *Proceedings of the National Academy of Sciences*, vol. 111, no. 36, pp. 13 004–13 009, 2014.

[71] C. R. Calladine, "Buckminster fuller's "tensegrity" structures and clerk maxwell's rules for the construction of stiff frames," *International journal of solids and structures*, vol. 14, no. 2, pp. 161–172, 1978.

[72] X. Mao and T. C. Lubensky, "Maxwell lattices and topological mechanics," *Annual Review of Condensed Matter Physics*, vol. 9, pp. 413–433, 2018.

[73] T. Lubensky, C. Kane, X. Mao, A. Souslov, and K. Sun, "Phonons and elasticity in critically coordinated lattices," *Reports on Progress in Physics*, vol. 78, no. 7, p. 073 901, 2015.

[74] R. Kangwai, S. Guest, and S. Pellegrino, "An introduction to the analysis of symmetric structures," *Computers & structures*, vol. 71, no. 6, pp. 671–688, 1999.

[75] R. Kangwai and S. Guest, "Symmetry-adapted equilibrium matrices," *International Journal of Solids and Structures*, vol. 37, no. 11, pp. 1525–1548, 2000.

[76] P. Fowler and S. Guest, "A symmetry extension of maxwell's rule for rigidity of frames," *International Journal of Solids and Structures*, vol. 37, no. 12, pp. 1793–1804, 2000.

[77] S. Guest and P. Fowler, "A symmetry-extended mobility rule," *Mechanism and Machine Theory*, vol. 40, no. 9, pp. 1002–1014, 2005.

[78] R. Kangwai and S. Guest, "Detection of finite mechanisms in symmetric structures," *International Journal of Solids and Structures*, vol. 36, no. 36, pp. 5507–5527, 1999.

[79] C. Kane and T. Lubensky, "Topological boundary modes in isostatic lattices," *Nature Physics*, vol. 10, no. 1, pp. 39–45, 2014.

[80] S. Guest and J. Hutchinson, "On the determinacy of repetitive structures," *Journal of the Mechanics and Physics of Solids*, vol. 51, no. 3, pp. 383–391, 2003.

[81] C. S. Borcea and I. Streinu, "Periodic frameworks and flexibility," *Proceedings of the Royal Society A: Mathematical, Physical and Engineering Sciences*, vol. 466, no. 2121, pp. 2633–2649, 2010.

[82] F. Bloch, "Über die quantenmechanik der elektronen in kristallgittern," *Zeitschrift für physik*, vol. 52, no. 7, pp. 555–600, 1929.

[83] D. Z. Rocklin, B. G.-.-.-g. Chen, M. Falk, V. Vitelli, and T. Lubensky, "Mechanical weyl modes in topological maxwell lattices," *Physical review letters*, vol. 116, no. 13, p. 135 503, 2016.

[84] D. Z. Rocklin, "Directional mechanical response in the bulk of topological metamaterials," *New Journal of Physics*, vol. 19, no. 6, p. 065 004, 2017.

[85] D. Z. Rocklin, S. Zhou, K. Sun, and X. Mao, "Transformable topological mechanical metamaterials," *Nature communications*, vol. 8, no. 1, pp. 1–9, 2017.

[86] B. G.-g. Chen, B. Liu, A. A. Evans, J. Paulose, I. Cohen, V. Vitelli, and C. Santangelo, "Topological mechanics of origami and kirigami," *Physical review letters*, vol. 116, no. 13, p. 135 501, 2016.

[87] M. Nakahara, *Geometry, topology and physics*. CRC press, 2018.

[88] K. Roychowdhury and M. J. Lawler, "Classification of magnetic frustration and metamaterials from topology," *Physical Review B*, vol. 98, no. 9, p. 094 432, 2018.

[89] K. Roychowdhury, D. Z. Rocklin, and M. J. Lawler, "Topology and geometry of spin origami," *Physical review letters*, vol. 121, no. 17, p. 177 201, 2018.

[90] H. Gluck, "Almost all simply connected closed surfaces are rigid," in *Geometric topology*, Springer, 1975, pp. 225–239.

[91] T. Tachi, "Rigid folding of periodic origami tessellations," *Origami*, vol. 6, pp. 97–108, 2015.

[92] H. Crapo and W. Whiteley, "Statics of frameworks and motions of panel structures: A projective geometric introduction," *Structural Topology, 1982, núm. 6*, 1982.

[93] J. McInerney, B. G.-g. Chen, L. Theran, C. D. Santangelo, and D. Z. Rocklin, "Hidden symmetries generate rigid folding mechanisms in periodic origami," *Proceedings of the National Academy of Sciences*, vol. 117, no. 48, pp. 30 252–30 259, 2020.

[94] B. G.-g. Chen and C. D. Santangelo, "Branches of triangulated origami near the unfolded state," *Physical Review X*, vol. 8, no. 1, p. 011 034, 2018.

[95] F. Feng, P. Plucinsky, and R. D. James, "Helical miura origami," *Phys. Rev. E*, vol. 101, p. 033 002, 3 Mar. 2020.

[96] A. Reid, F. Lechenault, S. Rica, and M. Adda-Bedia, "Geometry and design of origami bellows with tunable response," *Physical Review E*, vol. 95, no. 1, p. 013 002, 2017.

[97] T. Tachi, "Simulation of rigid origami," *Origami*, vol. 4, pp. 175–187, 2009.

[98] W. Finbow, E. Ross, and W. Whiteley, "The rigidity of spherical frameworks: Swapping blocks and holes," *SIAM Journal on Discrete Mathematics*, vol. 26, no. 1, pp. 280–304, 2012.

[99] H. Kedia, A. Souslov, and D. Z. Rocklin, "Soft topological modes protected by symmetry in rigid mechanical metamaterials," *Physical Review B*, vol. 103, no. 6, p. L060104, 2021.

[100] M. Stavric and A. Wiltsche, "Quadrilateral patterns for rigid folding structures," *International journal of architectural computing*, vol. 12, no. 1, pp. 61–79, 2014.

[101] T. A. Evans, R. J. Lang, S. P. Magleby, and L. L. Howell, "Rigidly foldable origami gadgets and tessellations," *Royal Society open science*, vol. 2, no. 9, p. 150 067, 2015.

[102] Z. He and S. D. Guest, "On rigid origami ii: Quadrilateral creased papers," *Proceedings of the Royal Society A*, vol. 476, no. 2237, p. 20 200 020, 2020.

[103] F. Lechenault, B. Thiria, and M. Adda-Bedia, "Mechanical response of a creased sheet," *Physical review letters*, vol. 112, no. 24, p. 244 301, 2014.

[104] B. H. Hanna, J. M. Lund, R. J. Lang, S. P. Magleby, and L. L. Howell, "Waterbomb base: A symmetric single-vertex bistable origami mechanism," *Smart Materials and Structures*, vol. 23, no. 9, p. 094 009, 2014.

[105] T. Jules, F. Lechenault, and M. Adda-Bedia, "Local mechanical description of an elastic fold," *Soft matter*, vol. 15, no. 7, pp. 1619–1626, 2019.

[106] B. Thiria and M. Adda-Bedia, "Relaxation mechanisms in the unfolding of thin sheets," *Physical review letters*, vol. 107, no. 2, p. 025 506, 2011.

[107] T. Jules, F. Lechenault, and M. Adda-Bedia, "Plasticity and aging of folded elastic sheets," *Physical Review E*, vol. 102, no. 3, p. 033 005, 2020.

[108] S. W. Grey, F. Scarpa, and M. Schenk, "Strain reversal in actuated origami structures," *Physical review letters*, vol. 123, no. 2, p. 025 501, 2019.